KfK 4485
Januar 1989

Chemical Interactions of Reactor Core Materials Up to Very High Temperatures

P. Hofmann, S. Hagen, G. Schanz, A. Skokan
Institut für Material- und Festkörperforschung
Hauptabteilung Ingenieurtechnik
Projektgruppe LWR-Sicherheit

Kernforschungszentrum Karlsruhe

Kernforschungszentrum Karlsruhe
Institut für Material- und Festkörperforschung
Hauptabteilung Ingenieurtechnik
Projektgruppe LWR-Sicherheit

KfK 4485

CHEMICAL INTERACTIONS OF REACTOR CORE MATERIALS UP TO VERY HIGH TEMPERATURES

P. Hofmann, S. Hagen, G. Schanz, A. Skokan

Kernforschungszentrum Karlsruhe GmbH, Karlsruhe

Kernforschungszentrum Karlsruhe GmbH
Postfach 3640, 7500 Karlsruhe 1

ISSN 0303-4003

Abstract

The paper describes which chemical interactions may occur in a LWR fuel rod bundle containing (Ag, In,Cd) absorber rods or (Al_2O_3/B_4C) burnable poison rods with increasing temperature up to the complete melting of the components and the formed reaction products. The kinetics of the most important chemical interactions has been investigated and the results are described. In most cases the reaction products have lower melting points or ranges than the original components. This results in a relocation of liquefied components often far below their melting points. There exist three distinct temperature regimes in which liquid phases can form in the core in differently large quantities. These temperature regimes are described in detail. The phase relations in the important ternary (U,Zr,O) system have been extensively studied. The effect of steel constituents on the phase relations is given in addition. All the considerations are focused on PWR conditions only.

Chemische Wechselwirkungen von Reaktorcorematerialien bis zu sehr hohen Temperaturen

Der Bericht beschreibt die möglichen chemischen Wechselwirkungen in einem LWR-Brennelement mit steigender Temperatur bis zum vollständigen Zusammenschmelzen. Berücksichtigt wird auch der Einfluß von (Ag,In,Cd)-Absorberstäben und von sogenannten "burnable poison rods", die B_4C in einer Al_2O_3-Matrix enthalten. Von besonderem Interesse war die Ermittlung der dominierenden chemischen Wechselwirkungen sowie der dazugehörigen Reaktionskinetik. In den meisten Fällen besitzen die entstehenden Reaktionsprodukte niedrigere Schmelzpunkte als die Ausgangskomponenten. Das hat zur Folge, daß die Komponenten z.T. weit unterhalb ihres Schmelzpunktes verflüssigt werden und sich dadurch leicht verlagern und in kälteren Bereichen Blockaden bilden können. Es existieren drei deutlich voneinander getrennte Temperaturbereiche in denen sich flüssige Phasen im Reaktorcore bilden; diese werden kurz beschrieben. Die Phasenbeziehungen in dem wichtigen ternären System (U-Zr-O) sowie der Einfluß von Stahlkomponenten auf die Phasenbeziehungen wurden umfassend untersucht.

Content

1. Introduction

In an unmitigated severe reactor accident, the UO_2 fuel and Zircaloy cladding may reach temperatures up to the melting point. With increasing fuel and cladding temperatures, fuel rod damage will occur in the core in a variety of forms. Since the various core components are thermodynamically unstable with each other chemical interactions will take place which become significant at temperatures above 1000 °C. To predict the material behavior in severe reactor accidents, a quantitative description of the different material interactions as a function of temperature and time is needed. For this reason, extensive out-of-pile single effects tests and integral experiments have been performed at the Kernforschungszentrum Karlsruhe (KfK) as part of the German Nuclear Safety Project to determine the reaction kinetics, to analyze and characterize fuel rod bundle damage and the formation of liquid phases.

In an unmitigated degraded core accident that leads to fuel rod melting and failure of the reactor core the following processes and chemical reactions can take place as the temperature rises (Figure 1):

- Plastic deformation and bursting or collapsing of the cladding, depending on the differential pressure during a low or high pressure accident scenario,
- Melting of the (Ag,In,Cd) alloy and, after failure of the stainless steel cladding, chemical interactions with Zircaloy,
- Formation of B_4C/stainless steel, Zircaloy/Inconel, Zircaloy/stainless steel and Zircaloy/Al_2O_3 eutectics,
- Oxidation and embrittlement of the cladding by H_2O (steam) and UO_2, which may result in rod fragmentation,
- Oxidation of the stainless steel and Inconel by steam,
- Melting of stainless steel and Inconel,
- Melting of the metallic Zircaloy cladding or the metallic oxygen-stabilized alpha Zircaloy [α-Zr(O) phase],
- Oxidation of the fuel by steam,
- Interactions between solid and/or molten Zircaloy and solid fuel, with partial dissolution and disintegration of UO_2, forming a metallic (Zr,U,O) melt, which may contain at higher oxygen concentrations ceramic $(U,Zr)O_{2-x}$ precipitations,
- Formation of an α-Zr(O)/zirconium dioxide (ZrO_2) eutectic,
- Melting of Al_2O_3 and B_4C,
- Eutectic and monotectic reactions between α-Zr(O) and UO_2,
- Melting of ZrO_2 and UO_2, forming a ceramic (Zr,U,O) melt,

- Formation of immiscible metallic and ceramic melts in different parts of the reactor core,
- Relocation of the solid and liquid materials into the lower pressure vessel (RPV) head, and
- Thermal and chemical attack of the RPV wall.

At temperatures above 1200 °C the rapid oxidation of Zircaloy and stainless steel by steam are additional important factors in a severe reactor accident because the heat generated by these exothermic chemical interactions resulta in local uncontrolled temperature escalations within the core with peak temperatures greater than 2000 °C. As soon as the Zircaloy cladding starts to melt (> 1760 °C) the solid UO_2 fuel may be chemically dissolved and thus liquefied about 1000 °C below its melting point. As a result, liquefied fuel relocation can already take place below 2000 °C.

Many of these physical and chemical processes have been identified in separate effects tests, out-of-pile and in-pile integral severe fuel damage (SFD) experiments, and TMI-2 core material examinations. All of these interactions are of concern in a severe accident, since relocation and/or solidification of the resulting fragments or melts may result in local cooling channel blockages of different sizes and may cause further heatup of these core regions because cooling still can be inadequate, causing further melt progression and material relocation into lower regions of the RPV.

Another phenomenon is the formation of rubble beds. The collapse of solid material onto the blockages (solidified materials and grid spacers) can form debris beds on top of the blockages. Continuous heatup of these debris beds can form molten pools, held in place by a solid crust, which acts as a crucible (as evidenced by TMI-2), with later crust collapse possibly influencing the late-melt relocation stage.

What is needed to analyze and describe the behavior of LWRs during a severe accident by an integral code is the relocation behavior of the various core materials, the hydrogen generation, the physical and chemical state of the core debris and its temperature prior to RPV failure, and the mode of vessel failure. Since the molten phases are formed at different temperatures during in-vessel core-melt progression, they will be formed in a complex pattern involving both spatial and temporal variations. As a result, the melt progression at different places in the core begins at different times. The various molten phases will

solidify on cooldown at different temperatures and will therefore form blockages at different axial locations. All these processes have a strong influence on hydrogen generation, natural circulation, the chemical composition of the melt in the lower head of the vessel and its temperatures. For this reason the material relocation processes have to be modelled and considered in the code systems as precisely as possible.

There exist three distinct temperature regimes in which liquid phases can form in the core in different quantities, either due to primarily eutectic chemical interactions or by reaching a melting point (range). These temperature regimes will be described in detail. In addition, the interaction determining processes, including the formation of liquid phases, will be quantitatively described (high temperature oxidation of the Zircaloy cladding by steam and UO_2 fuel; chemical interactions of the reaction couples Zircaloy/Al_2O_3, Zircaloy/(Ag,In,Cd), Zircaloy/stainless steel; and dissolution of UO_2 and ZrO_2 by molten Zircaloy). The phase relations in the important ternary (U,Zr,O) system have been extensively studied and provide an excellent basis for a better understanding and interpretation of the in-vessel core-melt progression phenomena which occurred during the TMI-2 accident and in out-of-pile and in-pile integral fuel rod bundle meltdown experiments.

2. Cladding material behaviour and interaction with the atmosphere

The chemical behaviour of the cladding is mainly determined by its oxidation in a steam environment in competition to its interaction with the UO_2 fuel pellets. The temperature dependence of the oxidation of Zircaloy-4 (Zry) in steam is very pronounced. This is the reason for the uncontrolled temperature escalation, which is mainly driven by the exothermal heat of the oxidation reaction. The elementary steps of the Zry/steam reaction are depicted in Figure 2 [1]. The pertinent mechanisms and the resulting kinetics are treated in the following.

2.1 Oxidation under unlimited steam supply

Under unlimited steam supply conditions, the reaction rate of Zry is determined by the oxygen transport through the pre-existent and growing substoichiometric ZrO_2 scale, whereas the presence of hydrogen as reaction product is only of

secondary importance. The consumed oxygen is partitioned between the scale, the underlying oxygen-stabilized α-Zr(O) layer and the β-Zr matrix. The steam consumption and the thickness of the oxygen-rich surface layers are increasing parabolically with time and with an exponential (Arrhenius-type) temperature dependence. At temperatures below 1100 °C the long-term oxidation kinetics of Zry is disturbed by the breakaway effect, the mechanical degradation of the oxide scale, which is connected with structural changes and results in typically linear growth of non-protective scales. The breakaway influence is unimportant in the present context, if the transient will leave the critical medium-temperature regime, since the scale defects tend to heal, and the growth of mechanically sound scales continues at higher temperatures (Figure 3 [2]). At high temperatures the oxidation kinetics of the Zry is influenced by the phase transformations of the ZrO_2 layer. Figure 4 shows the Zr-oxygen equilibrium phase diagram. At about 1525 °C the formation of an oxide sub-layer of cubic structure with higher oxygen diffusivity results in a nearly stepwise increase of the reaction rate. Within the two-phase range of tetragonal plus cubic ZrO_2 (between 1525 and 2285 °C) and at temperatures above, the reaction rate can be described again by an Arrhenius law [3] (Figure 5 and 6).

2.2 Interrelation between cladding oxidation and melting

With the onset of melting of the Zry cladding above about 1760 °C, the eutectic interaction of ZrO_2 and α-Zr(O) above 1900 °C, and the completed melting of α-Zr(O) at about 1975 °C (Figure 4), liquid phase formation disturbs the regular sequence of diffusion-caused reaction layers, and due to higher oxygen solubility and diffusivity in the melt, the oxygen concentration profile within the solid metallic part of the system levels out faster. The kinetic consequences for the oxidation, however, are not pronounced enough to be detected, according to the experimental results of Prater and Courtright (Figure 5 [3]). This investigation has confirmed the scatter band of available kinetic data in the lower temperature regime (Fig. 6 [4]), whereas it is the only study performed at extremely high temperatures. This lack of data is due to the increasing difficulty of the experimental procedure and data evaluation with increasing temperature. The reliability of the Prater and Courtright data seems adequate, since melt relocation forms fresh surfaces and reduces the area of originally exposed surfaces. Thus, the changing area of exposure contributes more and more to the uncertainty of the total oxygen mass consumption and heat production.

Another aspect of steam exposure of fresh metallic surfaces is that it can initiate repeated local temperature escalations.

2.3 Oxidation under limited steam supply

Under the conditions of limited steam supply, the Zry oxidation differs from the above characterization with respect to both mechanistic and kinetic aspects. In this case of "steam starvation" the oxidation process consumes totally the steam available to the surface, so that the reaction rate is determined by the transport properties of the gas phase. Interdiffusion along the respective concentration gradients of the consumed steam and the rejected hydrogen results in a linear time dependence of the oxidation rate. The critical steam flow rate per area of oxidizable material, below which steam starvation can be detected, has been determined up to 1400 °C (Figure 7) [5].

A serious lack of available steam is accompanied by exchange of oxygen from the oxide scale to the underlying metal, by which the oxygen gradients tend to level off. In the extreme case, without any further oxidation, oxide scales can be completely dissolved, provided that sufficient metal is present to absorb the oxygen. One consequence of such an oxide scale dissolution is the initiation of cladding melt relocation (Figure 8), since the ZrO_2 layer, which held the melt at place, disappears.

2.4 Consideration of hydrogen

The influence of hydrogen on oxidation kinetics under limited steam supply has been of some interest. The earlier proposed retarding effect of hydrogen on the oxidation of Zry [1] has not been confirmed by more recent investigations. However, during the slow growth of thin oxide scales or in case of the above mentioned scale dissolution, hydrogen may act as competitive reactant, as long as its solubility in the alloy is not reached. Whereas the latter is known to decrease with increasing temperature, it increases with the square root of the hydrogen partial pressure in the surrounding atmosphere. The dissolved hydrogen is equally distributed in the matrix due to its high diffusivity. Hydride phases are not stable at the high temperatures of concern. Since the hydrogen solubility of ZrO_2 is negligible, oxidizing hydrogen saturated material will finally change from the character of a hydrogen sink to that of a hydrogen source, so that the gross effect of hydrogen absorption of Zry remains limited [4].

2.5 Analytical treatment of the Zircaloy oxidation

The Zry/steam reaction should be treated by a mechanistic code instead of the simple basis of rate laws presented above, since those are disturbed when the complete oxidation of the material is approached. The code PECLOX [6] is able to calculate the Zry cladding oxidation, that means steam consumption as well as layers growth, for given temperature transients on the basis of Zry-O (Zr-O) phase diagram information (Figure 4) and oxygen diffusivities. The competing oxidation in contact with the fuel pellet is treated in parallel (see chapter 4). Implemented into code systems it would contribute to improve the reliability of temperature calculations. In order to treat oxidation under steam starvation conditions with the code the supply rate of available steam is used as input. The code results can be easily translated into information on heat and hydrogen evolution.

The phenomenological basis for the treatment of Zry/hydrogen interaction by a code is provided, as described above. However, hydrogen solubility data for oxygen-containing Zry are not available.

2.6 Zircaloy cladding material embrittlement

Different aspects of the embrittlement, induced by the oxidation of the cladding material have to be distinguished [7]. One is the reduced circumferencial rupture strain of internally pressurized cladding, which is due to strain concentration and early necking below cracks through the oxide scales. Another aspect is related more closely to the oxygen content of the alloy itself: On the basis of fundamental embrittlement investigations and in order to prevent "fuel rod shattering", the 17 % oxidation limit had been established as large break LOCA licensing criterion. More recent studies [8] have demonstrated, that retained cladding ductility with respect to loads from quenching and handling is dependent on a minimum residual thickness of cladding with a sub-critical oxygen content. In addition to the embrittling influence of the oxidation, increased hydrogen contents are effective in a similar way at lower temperatures [7].

Embrittlement at high temperatures is much less defined and investigated. Low-temperature brittleness of the ZrO_2 and α-Zr(O) phases with respect to applied

stresses gives way to increasing ductility of those phases with increasing temperature, especially under slowly developing loads.

During their growth substoichiometric oxide scales are more able to accommodate stresses by diffusion mechanisms than are stoichiometric oxide shells. However, oxidation-induced stresses increase in importance with rising temperature. The respective stress or deformation of the cladding is related to the high volume ratio of oxide to consumed metallic matrix (Pilling-Bedworth ratio; about 1.5). This intrinsic loading mechanism is able to explain the so-called flowering phenomenon of Zry cladding by tensile oxidation stresses in the metallic matrix, differences in the oxygen consumption around the cladding circumference, and the time lag of the internal steam oxidation. In combination this leads to tube growth, longitudinal tube splitting, bending and flattening. The cladding deformations continue until total conversion of the metal to oxide is achieved.

Extrinsic loading mechanisms are axial fuel rod constraint, temperature gradients and resulting bending, tube contact with refrozen melt or surrounding structures, dynamic forces from atmosphere, melts or quench water. Mainly the dynamic forces are expected to lead to finer cladding fragmentation and rubble bed formation. Static loads alone will typically result in localized cracking of still coherent larger fragments.

3. Oxidation of stainless steel by steam

The oxidation behavior of stainless steels in a steam environment will be briefly discussed and compared with that of Zry. Since no information in the SFD context is available, the following discussion is based on kinetics data of experimental work performed under safety considerations of an Advanced Pressurized Water Reactor (APWR) using stainless steel for the cladding of the fuel rods [9,10].

The austenitic 15Cr15Ni stainless steel (DIN Material No. 1.4970) showed in mechanical testing a decrease in ductility which was similar to that observed with Zircaloy, and which was due to cracks through the defective oxide scale. The scales forming at 1000 - 1300 °C were found to be composed essentially of a Cr-rich protective internal sublayer and a porous Fe-rich external layer of less protective character. The kinetics of oxygen uptake and scale growth could be

described by parabolic rate constants with Arrhenius-type dependence on temperature. In comparison with Zircaloy-4 the stainless steel oxidized equally fast at 1300 °C and more slowly at temperatures below. The experimental results are shown in Figure 9.

The oxidation of the ferritic/martensitic 12Cr steel (DIN Material No. 1.4914) was characterized by the growth of similar subscales. At higher temperatures the scales showed a faceted surface due to fast oxide grain growth. The oxidation was measured to be faster than that of the austenitic steel and the Zircaloy-4 (Figure 9).

The oxidation kinetics of stainless steels is not expected to depend strongly on the type of material. Ni-based alloys as Inconel are known to behave similarly. The temperature dependence of the oxidation rate seems to be slightly higher than that of Zircaloy. Whereas the melting of the steel matrix is not judged to be of great influence, the melting of the oxide scales at about 1500 °C will terminate the regime of simple analytical treatment of steel oxidation.

4. Chemical interaction between UO_2 fuel and Zircaloy-4 cladding material

Beside the oxidation of the cladding from the outside by steam oxidation of the cladding from the inside by the UO_2 fuel will occur, especially at higher temperatures. This oxygen uptake provides a considerable contribution to cladding embrittlement. Above the melting point of the Zircaloy-4 cladding ($\approx$ 1760 °C) the solid UO_2 fuel will be chemically dissolved (liquefied) about 1000 K below its melting point. The essential results of the chemical interactions of solid UO_2 fuel with solid and liquid Zry are described in the subsequent chapters.

4.1 Interactions between UO_2 and solid Zircaloy

The results of the UO_2 fuel/solid Zry reaction experiments under isothermal and transient temperature conditions have been extensively described in [11,12]. The results show that due to oxygen uptake by the Zry cladding from reaction with gaseous oxygen or steam on the outside and from reaction with UO_2 on the inside oxygen stabilized α-Zr(O) phases, ZrO_2 and a metallic (U,Zr) alloy form. The sequence of the various phases or reaction layers, starting from the inside

surface, for isothermal and transient temperature experiments at all temperatures is:

$$[UO_2 + U] \rightarrow [\alpha - Zr(O)_a + (U,Zr)^*] \rightarrow [U,Zr]\,alloy \rightarrow \alpha - Zr(O)_b \rightarrow \beta - Zry \rightarrow \alpha - Zr(O)_c \rightarrow ZrO_2$$

* The (U,Zr) alloy within the α-$Zr(O)_a$ layer is concentrated mainly at the grain boundaries, but also exists within the matrix.

Figure 10 shows the sequence of the external and internal interaction layers. The α-$Zr(O)_{a,b}$ layers forming on the inside of the cladding and the α-$Zr(O)_c$ layer forming on the outside of the cladding grow at roughly the same rates. Moreover, due to the elevated oxygen potential (oxygen partial pressure) of the gas mixture or steam compared to stoichiometric UO_2, a ZrO_2 layer also forms on the external cladding surface. Initially, the growth of the reaction layers obeys parabolic rate laws. However, since the wall thickness of the cladding is small (0.72 mm), the tubing must be considered as a finite system. For this reason, the external and the internal oxygen uptake influence each other and an accelerated growth of the reaction layers is observed at longer reaction times, especially after the β-phase has disappeared.

With increasing time the β-phase of the cladding disappears due to oxygen uptake and transformation into α-Zr(O). After the disappearance of the β-phase, the oxidized cladding tube is completely embrittled and is no longer mechanically stable. The slightest force exerted during cooling, quenching or subsequent handling causes the fuel rod sections to break apart. Since embrittlement of the cladding occurs as a result of the formation of oxygen-stabilized α-Zr(O), the internal oxidation makes approximately the same contribution as the external oxidation. For this reason, embrittlement of the cladding occurs about four times faster than by one-sided oxidation alone. Further oxidation of the cladding results in a complete transformation of the α-Zr(O) into ZrO_2.

A comparison of the parabolic growth rate equations of the whole reaction zones for the UO_2/Zry, O_2/Zry, and H_2O/Zry chemical interactions is shown in Figure11. Note that the total UO_2/Zry growth rate curve overlaps the steam/Zry region (results of six investigations [11,12] above about 1100 °C. This means that the UO_2/Zry reaction occurs as rapidly as the steam/Zry reaction above about 1100 °C.

4.2 Analytical treatment of the UO_2/Zircaloy interactions

The modelling of the combined internal and external cladding interactions resulted in the PECLOX (pellet cladding oxidation) numerical model. PECLOX solves the Fick and Stefan equations. It predicts the formation, growth, and disappearance of the various interaction layers and the corresponding oxygen profiles as a function of temperature and time up to complete Zry cladding oxidation [6,13]. In this respect, the PECLOX model has major advantages over other models [14,15], which attempt only to simulate the kinetics of the system in the first stages of the process, when all interface movements obey parabolic rate laws (infinite systems). Figure 12 shows a comparison between experimental results and calculations for an isothermal fuel/cladding interaction experiment under oxidizing conditions at 1100 °C. The phase boundary movements (altogether six interfaces) are plotted versus the square root of time. The agreement between experiment and calculation is satisfactory [13].

Figure 13 shows as an example the calculated oxygen concentration profiles for the combined cladding interactions at 1100 °C after 3000 and 10000 seconds reaction time. Oxygen diffuses into the Zircaloy cladding from the inside and the outside forming various interaction layers. The metallic (U,Zr) alloy forming between the two oxygen stabilized α-$Zr(O)_{a,b}$ layers contains only a small amount of oxygen. The β-phase saturates with oxygen (3000 s) and then finally disappears. After long reaction times the cladding will be completely converted to ZrO_2 since the oxyen potential (oxygen partial pressure) is higher on the outside (O_2 or H_2O) than on the inside (UO_2). The (U,Zr) alloy then transforms into a $(U,Zr)O_2$ oxide. Swelling due to a density change of the reaction products occurs at the ZrO_2/α-$Zr(O)_c$ interface. This results in an increase of the overall diameter of the fuel rod segment (Figure 12), which is considered in PECLOX.

4.3 UO_2 Dissolution by molten Zircaloy

The meltdown behavior of Zry cladding depends decisively on the extent of the cladding oxidation and on the possible formation of a ZrO_2 oxide layer during the heating period. However, the oxygen uptake by Zry depends not only on the oxygen potential of the environment but also on the chemical interaction with the UO_2 fuel, which is determined by the fuel/cladding contact conditions, i.e., the external overpressure [16]. Under non-oxidizing conditions the Zry cladding

will relocate as soon as melting occurs and will dissolve some UO_2. The relocation of the liquid Zry depends on the wetting behavior which is determined by the oxygen concentrations in the melt [28]. Under oxidizing conditions an oxide layer forms on the outer cladding surface during heating before the melting point of Zry or α-Zr(O) has been reached. Therefore, the relocation of molten material will be prevented. The molten Zry cladding then interacts with UO_2 and the ZrO_2 shell.

UO_2 and ZrO_2 are dissolved chemically by the molten metallic Zry cladding material, i.e. they are liquefied. This causes relocation of UO_2 and ZrO_2 well below their melting points (about 1000 K). In the cooler lower part of the reactor core the solidified melts can give rise to cooling channel blockages of different sizes.

While UO_2 is dissolved by liquid Zircaloy, a (U,Zr,O) melt is formed which decomposes into two metallic phases and one ceramic phase during cooldown. When ZrO_2 is dissolved the (Zr,O) melt formed decomposes into a metallic and a ceramic phase. The ceramic phases are formed only above a critical oxygen concentration in the melts and depend on the amount of dissolved UO_2 or ZrO_2. The ceramic phase portion in the solidified melts is used to quantify the extent of chemical dissolution of UO_2 and ZrO_2, respectively. The kinetics of chemical UO_2 and ZrO_2 dissolution by molten Zircaloy follows parabolic rate laws [17]. The activation energy is approximately the same for both processes (Figure 14). The rate of UO_2 dissolution is distinctly higher than the rate of ZrO_2 dissolution.

In general, the dissolution of solid fuel by molten Zircaloy is very fast; at 2250 °C after 5 minutes the solidified (Zr,U,O) melt consists of about 80 wt% of dissolved UO_2 (Figure 14; initial molten Zry weight to melt/solid UO_2 contact area: $\approx$ 1.7) [17]). The amount of UO_2 which can be dissolved depends on the quantity, initial oxygen content, and temperature of the Zircaloy melt. As the initial oxygen content of the metallic Zircaloy melt increases, the amount of UO_2 which can be dissolved by the melt decreases.

Under oxidizing reactor conditions, the Zircaloy also picks up oxygen from the steam. The chemical interaction between Zircaloy and UO_2 will therefore not be as extensive as in an inert environment; this was experimentally demonstrated by Kim and Olander [29]. In a severe reactor accident, however, a non-oxidizing atmosphere could exist in the upper core region. At very high cladding

temperatures, the steam entering the lower core region could completely react with Zircaloy to form α-Zr(O), ZrO_2, and hydrogen, leaving a non-oxidizing atmosphere in the upper core region for some time during the transient.

In all the fuel dissolution experiments a strong disintegration of parts of the solid UO_2 crucible was observed after a specific reaction time. The disintegration can be explained as follows. The UO_2 is reduced by the Zircaloy to hypostoichiometric UO_{2-x}. If the fuel is reduced below the UO_{2-x} / (UO_{2-x} + U) phase boundary, metallic uranium (liquid above 1130 °C) forms in the UO_{2-x}, preferably along the grain boundaries. If a specific amount of uranium in the UO_{2-x} structure is exceeded, the fuel structure disintegrates. The fuel particles are then dispersed in the melt and, because of their large surface area, rapidly dissolved. By this process, the fuel is "liquefied" far below its melting point. The process of the UO_2 disintegration at the solid/liquid interface can be easily recognized in Figure 15; the dispersed fuel particles have grain or subgrain size. The disintegrated solid fuel particles will be subsequently chemically dissolved by the liquid Zircaloy. Due to the high temperatures involved and the strong affinity of Zircaloy for oxygen the inital stoichiometric UO_2 will be reduced to hypostoichiometric fuel (UO_{2-x}). At the same time, a limited Zr diffusion into the UO_{2-x} takes place, forming a $(U,Zr)O_{2-x}$ solid solution as an intermediate compound before it is completely dissolved. With increasing amount of UO_2 dissolved in the (Zr,U,O) melt the oxygen concentration increases until the temperature-dependent oxygen solubility limit has been reached. Further dissolution of UO_{2-x} results then in the formation of $(U,Zr)O_{2-x}$ precipitates at temperature. Additional $(U,Zr)O_{2-x}$ precipitates will form on cooldown of the (Zr,U,O) melt. The hypostoichiometric UO_{2-x} and $(U,Zr)O_{2-x}$ decompose on cooldown into $UO_{2.00}$ + U and $(U,Zr)O_{2.00}$ + α-Zr(O).This experimental observation is the basis for the proposed dissolution model described in the following chapter.

4.4 Analytical treatment of the UO_2 dissolution

Since an analytical solution for the UO_2 fuel dissolution by molten Zry can be very difficult, a numerical solution (code) was developed: LISI (Liquid Zircaloy - Solid Uranium Oxide Interaction). One of the essential assumptions of the model is that the UO_2 dissolution by molten Zircaloy is controlled by an oxygen diffusion process in the liquid. The solid UO_2/molten Zircaloy reaction interfacial area increases due to UO_2 dissolution and disintegration. To simulate this process an artificially high equivalent oxygen diffusion coefficient was considered in the

liquid near the interface. The equivalent oxygen diffusion coefficient approaches its true physical value in the molten Zircaloy far away from the solid/liquid reaction interface. The high activation energy involved in the UO_2/molten Zircaloy interaction is correlated with the increased oxygen diffusion coefficient near the UO_2/Zircaloy interface. The LISI [17] code can determine the oxygen concentration profile and the interface position at every time and is able to predict the dissolution rate of UO_2 at each temperature. A comparison between experimental results and LISI model calculations is shown in Figure 16; there exists a good agreement between numerical results and experimental data.

In the LISI code it is assumed that the diffusion of oxygen in the Zry melt is the rate determining process of the UO_2 dissolution, whereas Kim and Olander [29] assumed that uranium diffusion in the molten Zry controls the fuel dissolution.

5. U-Zr-O high-temperature phase relations

The first investigations of the phase stability relations in the ternary U-Zr-O system were performed by Saller et al. [18] who proposed three tentative isothermal sections at temperatures up to about 1100 °C. Further investigations were done by Politis [19] who determined the melt and phase equilibria in isothermal sections at 1000, 1500 and 2000 °C and the quasibinary section between UO_2 and oxygen-saturated α-Zr, which was designated Zr(O). Later on, the phase relations between 1500 and 2000 °C were investigated experimentally by Skokan [20] with the aim to clarify some contradictions between the isothermal sections and the temperature concentration diagram of the quasibinary join α-Zr(O)-UO_2, as well as to determine the liquidus curves in isothermal steps of 100 °C between 1500 and 2000 °C. Computational work on this system was done by Miyake et al. [21].

5.1 Ternary isothermal U-Zr-O sections

The most important features of this ternary system are the existence of an extended central three-phase region [UO_2 + α-Zr(O) + (U-Zr) solid solution or melt]. UO_2 is stable with oxygen-saturated α-Zr(O), but not with β-Zr. With regard to the UO_2-Zr interaction this result explains the observed ternary chemical interaction by which uranium oxide is partially reduced to uranium metal as long as zirconium is not saturated with oxygen. With increasing

temperature, the field of the (U-Zr) melt extends toward Zr [22] and thus the concentration of the liquid phase in the central three-phase field changes likewise (Figure 17 and 18). Since at temperatures > 1525 °C cubic ZrO_{2-x} is coexisting with α-Zr(O) (Figure 4) [23], a complete range of miscibility between UO_{2-x} and ZrO_{2-x} can be assumed resulting in a large two-phase field $(U,Zr)O_{2-x}$ + α-Zr(O) (Figure 18) instead of a three-phase field UO_{2-x} + ZrO_{2-x} + α-Zr(O) that exists below 1525 °C.

5.2 Ternary temperature-concentration diagrams

Considering the phase relations of the diffusion couple UO_2-Zr, it is certainly advantageous to show not only the diagram of the quasibinary equilibrium system α-Zr(O)-UO_2 but also additional temperature concentration diagrams representing the phase relations at different oxygen potentials or oxygen concentrations in the Zr. Therefore the diagrams of the ternary joins $Zr_{0.5}O_{0.5}$-UO_2, $Zr_{0.7}O_{0.3}$ [α-Zr(O)]-UO_2 and Zr-UO_2 are shown in the Figure 19. For a direct comparison with the isothermal ternary sections the concentrations are given in at.-% (the sum of all elements then is always 100). One can recognize that due to the reaction between Zr and UO_2 a metallic, U and Zr containing melt forms already below 1500 °C which does not form in the quasi binary system α-Zr(O)-UO_2.

The measured eutectic temperature of the quasibinary Zr(O)-UO_2 system is in accordance with the α-Zr(O)-ZrO_2 eutectic temperature of the binary Zr-O system, measured by Domagala [24] and Gebhardt [25] (1900 °C), whereas Ackerman [26] reported a significantly higher value for the Zr-O eutectic temperature. Very often the phase relation in the system α-Zr(O)-UO_2 is used and interpreted in a wrong way. It can only be used when oxygen saturated α-Zr(O) is in contact with UO_2. Small deviations in the oxygen concentration of the Zr result in different phase formations and stabilities. This is especially true with respect to the eutectic temperature and the eutectic point. Figure 20 shows the quasibinary system α-Zr(O)-UO_2 in mol.% together with typical microstructures of melt specimens with hypoeutectic, eutectic [α-Zr(O)/UO_2] and hypereutectic compositions. The eutectic point in the quasibinary system α-Zr(O)-UO_2 lies at about 15 mol.% UO_2. The maximum amount of UO_2 which can be completely dissolved at 2000 °C is about 16 mol.% UO_2, forming a homogeneous (Zr,O.U) melt. However, about 80 mol.% UO_2 can be disintegrated at 2000 °C under the

formation of a heterogeneous melt consisting of a (U,Zr,O) liquid and solid $(U,Zr)O_{2-x}$ particles (Figure 20).

In the diagram of the ternary join $Zr_{0.5}O_{0.5}$-UO_2 (Figure 19). The homogeneous liquid phase field of the $Zr_{0.7}O_{0.3}$-UO_2 diagram does not exist any more. On the UO_2-rich side the $(U,Zr)O_{2-x}$ one-phase field extends to lower UO_2 contents.

5.3 Effect of steel constituents on the U-Zr-O phase relations

For the consideration of melting reactions, the quaternary U-Zr-Fe-O system may be regarded as a model system for the complicated multi-component system of a beginning core melt. The sections UO_2-Zr-Fe and $(U_{0.5}Zr_{0.5})$-Fe-O, shown schematically in Figures 21 and 22, represent the most relevant phase relations with respect to the core materials interactions, e.g. between Zircaloy cladding and Inconel spacer grid and between molten fuel rod and structural steel materials. The ternary sections UO_2-Zr-Fe and UO_2-Zr(O)-Fe were assessed for 1500 °C (Figures 23 and 24) on the basis of the subsystems Zr-Fe-O, U-Fe-O [27] and U-Zr-O (see above) and from additional experiments at KfK. The phase relations in both sections that have to be regarded for different oxygen potentials are very similar. At lower oxygen potentials (section UO_2-Zr-Fe, Figure 23) the liquid phase regions are more extended, and at higher oxygen potentials (section UO_2-Zr(O)-Fe, Figure 24) ZrO_2 as an additional solid phase appears in the corresponding phase fields. At higher temperatures, e.g. 2000 °C, a large two-phase field $(U,Zr)O_{2-x}$ + L and extended liquid metal phase fields (rich in Fe or in Zr) exist in both sections.

The phase relations of a characteristic core melt at very high temperatures (2500 °C) are tentatively shown in Figure 25 as a function of the iron and oxygen concentrations. Varying compositions of the core melt are marked by the points A, B, C, ..., G, corresponding to the increasing amount of steel components and to different states of oxidation of the components in the course of the core melt down accident.

6. Reaction behavior of burnable poison rods, absorber rods and Inconel spacer grids

The main components in a reactor core are UO_2 and Zry which make up about 92 wt.%. The remaining 8 % are primarily stainless steel, Inconel, (Ag,In,Cd) absorber rod material, and Al_2O_3, which is used in burnable poison rods [30]. The elements U, Zr, Fe, Cr, Ni, Ag, In, and Al comprise over 98 % of the total core and they will determine, together with oxygen in the chemical form of UO_2, Al_2O_3 and H_2O, the reaction behavior of the various components during a severe reactor accident. Beside the interactions of the initial components with each other the interactions between the reaction products also have to be considered. Of concern is the formation of low-temperature liquid phases which may relocate and form local blockages which result in a further heatup of the core.

What is primarily needed is the time-dependent information on the physical and chemical state of the various core components, the temperature distribution within the core, the hydrogen generation, and fission product release up to the failure of the reactor pressure vessel. In the following chapters the reaction behavior and failure mechanisms of the most important core components: a) burnable poison rods, b) absorber rods, and c) spacer grids with respect to Zry cladding will be briefly described as a function of temperature. Separate-effects tests have been performed in parallel to the integral out-of-pile and in-pile experiments and serve to explain the complex material interactions in the integral tests and the TMI-2 accident by the resulting multi-phase system at room temperature. In some cases a complete interpretation of the interactions will not be possible. However, in many cases statements with respect to the maximum temperature reached will be possible.

6.1 Chemical interactions between Al_2O_3 and Zircaloy

A mixture of Al_2O_3 and about 1.4 wt.% B_4C is used in some PWR as burnable poison rod material. B_4C acts as neutron absorber and reduces the initial high excess reactivity of fresh fuel rods. In the TMI-2 core 72 fuel assemblies out of 177 contained 16 burnable poison rods each. The Al_2O_3 weight was about 630 kg.

In the TMI-2 accident the burnable poison rod fuel assemblies showed increased damage. The upper end fittings region of the burnable poison fuel assemblies especially appears to have incurred more damage than the adjacent control rod

fuel assembly upper end fitting region [30]. The cause of the increased damage may be the effect of chemical reactions between Al_2O_3 and the Zircaloy-4 cladding of the burnable poison rods. To determine if Al_2O_3/Zircaloy chemical interactions cause a low-temperature failure of the burnable poison rod fuel assemblies due to early melt formation and melt propagation out-of-pile integral (CORA B and C test [32]) and separate-effects tests have been performed.

As a result of Al_2O_3/Zry chemical interactions a rather complicated pattern of reaction layers form, some of which are very small and can only be recognized by SEM studies at high magnifications. The type of reaction zones depends on temperature. Figure 26 shows the metallographic appearance of the overall reaction zone at 1400 °C after 30 min. Between 1300 and 1400 °C the formed (Al,Zr) eutectic alloy becomes liquid and partially relocates. The diffusion of Al into the Zry reduces the onset of melting from 1760 to about 1350 °C (eutectic between β-Zr and $AlZr_2$). At 1500 °C, the (Al,Zr) eutectic alloy, which contains also some oxygen, seems to be completely molten. The growth of the interaction zones obeys parabolic rate laws. The results of the kinetics data evaluation are plotted in Figure 27; shown is the reaction zone growth rate as function of reciprocal temperature (Arrhenius diagram). Literature data and the chemical diffusion coefficient of oxygen in α-Zr(O) are plotted in addition [31]. The kinetics of the Al_2O_3/Zry interactions seems to be controlled by the diffusion of oxygen into Zry. The sudden increase of the reaction zone growth rate at about 1400 °C may be caused by the formation of liquid phases around this temperature. At temperatures ≥ 1550 °C the specimens were completely liquefied during heatup, i.e. about 200 °C below the melting point of β-Zry and even further away from the melting point of Al_2O_3 (2050 °C). This observation is in agreement with the results of the CORA tests B and C where Al_2O_3 pellets were used instead of UO_2 pellets [32]. Failure of the Al_2O_3/Zry test rods started at 1350 °C when the first droplets of molten material were observed running down the test bundle forming blockages upon solidification. The process of liquefaction is initiated by a reduction of Al_2O_3 by Zry resulting in a (Zr,Al,O) melt which decomposes on cooldown into two metallic phases, a (Zr,Al) alloy and α-Zr(O) [32]. Above 1500 °C strong melt formation and relocation could be noticed in the tests CORA B and C.

Al_2O_3 interacts eutectically with UO_2 and/or ZrO_2 forming typical microstructures which have also been seen during TMI-2 core fragment and core bore

examinations. The eutectic temperatures are well below 2000 °C [33]. These low-temperature melt formations may be an explanation of the early failure of the burnable poison rod fuel assemblies in the TMI-2 core.

6.2 Chemical interactions between the absorber rod alloy (Ag,In,Cd) and Zircaloy

The absorber rod alloy (80 wt.% Ag, 15 % In, 5 % Cd) is thermodynamically stable with its stainless steel cladding, even in the liquid state. However, the absorber rod guide tube is made from Zry which will chemically interact with the stainless steel cladding of the absorber rod. During a severe reactor accident localized contact between stainless steel and Zry will exist at many places. This solid state contact results in chemical interactions with the formation of liquid phases around 1150 °C (see chapter 6.3). After failure of the absorber rod cladding the molten (Ag,In,Cd) alloy (melting point ≈ 800 °C) will come into contact with the Zry guide tube and will chemically destroy it. Then, the molten (Ag,In,Cd) can even attack and chemically dissolve the Zry cladding of the fuel rods well below the melting point of Zry (≈ 1760 °C). The relocating (Ag,In,Cd) alloy is therefore able to propagate and accelerate the core melt progression at rather low temperatures.

Figure 28 shows the interaction zone of two Zry/(Ag,In,Cd) specimens after annealing at 1000°C/5 min and 1150 °C/2 min. One can recognize that the Zry cladding is chemically dissolved by the molten absorber rod alloy by the formation of a homogeneous alloy which decomposes on cooldown into various phases. The reaction zone growth rate is plotted in an Arrhenius diagram versus the reciprocal temperature in Figure 29. At temperatures above 1200 °C the chemical interactions result in a sudden and complete liquefaction of the compatiblity specimens. As a consequence, the Zry cladding can be chemically dissolved about 600 °C below its melting point and may result even in a low-temperature UO_2 fuel dissolution.

6.3 Chemical interactions between Zircaloy and stainless steel

The Zry/stainless steel interactions are important with respect to the absorber rod cladding/Zry guide tube contact and the Inconel spacer grid/Zry fuel rod cladding contact. In both cases, early-melt formation has to be expected which initiates the melt progression within the fuel assembly at low temperatures.

Figure 30 shows the reaction zones which form as a result of the Zry/stainless steel interactions. Liquid phases form already at low temperatures, however, the reaction kinetics becomes significant only above 1100 °C. This could be recognized in the CORA tests where fuel rod bundles were heated up to complete meltdown. In all cases, the damage of the bundle was initiated due to Zry/Inconel interactions, which are similar to Zry/stainless steel interactions. Localized liquefaction of these components started around 1200 °C.

The reaction kinetics between Zry and stainless steel can be divided into a reaction zone growth rate in Zircaloy and one in stainless steel. The results are plotted in Figure 29. One can recognize that the Zry is attacked more strongly than the stainless steel. Oxide layers on the Zry cladding OD delay the chemical interactions between Zry and steel, but they cannot prevent it. The influence of oxide layers becomes less important at temperatures above 1100 °C.

7. Meltdown behaviour of PWR fuel rod bundles

Beside in-pile experiments in the ACRR, NRU, NSRR, PBF and Phebus, out-of-pile bundle experiments have been performed in the NIELS and CORA facility to investigate the integral meltdown behaviour of fuel rod bundles, the formation of blockages due to melt relocation and solidification and the formation of rubble beds on cooldown or during quenching. 25 rod bundles of 2 m length are used in the CORA facility [34]. The decay heat is simulated electrically by central tungsten heaters which are surrounded by annular UO_2 pellets and the Zry cladding. 16 rods are heated, 9 rods are unheated and contain solid UO_2 pellets. To study the influence of various bundle components on the meltdown behaviour, Inconel spacer grids, in addition to Zry spacer grids, were used. Some of the CORA test bundles contained one or two (Ag,In,Cd) absorber rods. The absorber material is clad in stainless steel tubes which are inside a Zry guide tube.

Altogether 6 CORA tests (B, C, 2, 3, 5, 12) have been performed to date. In the tests CORA B and C Al_2O_3 pellets were used instead of UO_2 pellets to study the high-temperature behaviour of burnable poison rods; the maximum temperatures were about 2000 °C [32]. The objectives of the CORA tests 2 and 3 were to get information on the behaviour of Inconel spacer grids in contact with Zry cladding. The maximum temperature within the bundle was in CORA 2 about 2000 °C and in CORA 3 about 2400 °C [35]. The test bundles CORA 5 and 12

contained in addition (Ag,In,Cd) absorber rods; the maximum temperatures in both tests were about 2000 °C. In CORA 12 the hot bundle was quenched by a rising water front [38].

Up to now the following preliminary results have been obtained: In all tests an uncontrolled temperature escalation took place beyond 1100 °C due to the exothermal Zry/steam interaction. The initial heatup rate of 1 K/s increased then to about 20 K/s. As a result of self limiting processes (growing ZrO_2 layers on the cladding outer surface and melt relocation) the temperature increase ceases at about 2000 °C if no additional electric power is supplied to the bundle. The rate of temperature increase has a strong impact on the extent of oxidation of the bundle components and the extent of liquid phase formation. The temperature at which melts form is strongly influenced by the Inconel spacer grids, absorber rods and burnable poison rods. The chemical interaction of these materials with the Zry cladding initiates the bundle damage and causes the UO_2 fuel dissolution far below the melting point of UO_2 ($\approx$ 2850 °C) and partially even below the melting point of Zry ($\approx$ 1760 °C).

In bundle tests without an absorber rod the melting starts at the elevation of the Inconel spacer grid due to eutectic interactions between Inconel and Zry. Relocation of the melts forms blockages at the lower end of the bundles. Fragmentation of fuel pellets to fine particles can occur during cooldown [35,36]. The higher temperatures in test CORA 3 compared to CORA 2 resulted in nearly complete meltdown of the Zry fuel rod cladding (free standing columns of declad fuel pellets stucked together at the pellet/pellet interfaces and cracks within the pellets by once molten Zry cladding, containing dissolved UO_2) with the formation of an extended blockage which nearly closed the whole cross-section.

Remarkably more molten material forms in the bundle with (Ag,In,Cd) absorber rods [37,38]. Melt movement within the bundle starts with the failure of the absorber rod and the resulting release of the (Ag,In,Cd) melt. Only a small amount of the absorber melt is moving down inside the gap between the guide tube and the absorber rod. The major part is radially and axially distributed within the bundle. The relocation of the absorber material in the bundle takes place mainly as rivulets. Only a minor portion falls down in form of fine droplets to the lower cold spacer grid. The absorber melt initiates the liquefaction of the fuel rod cladding. The Zr in the resulting melt starts the chemical dissolution of

the UO_2 pellets. The melts contain various amounts of dissolved UO_2 and they relocate in the lower part of the bundle. Figure 31 shows at the 500 mm elevation of the CORA bundle 5 how the molten (Ag,In,Cd) alloy comes into contact with the Inconel grid spacer, which is still intact (upper picture). Due to chemical interactions with the absorber melt the grid spacer becomes chemically dissolved and finally disappears (Figure 31, lower picture).

Figure 32 shows the post-test appearance of the CORA bundle 5 and Figure 33 a magnification of the center region. One can recognize the embrittled cladding, relocated melts and UO_2 fragments. The vertical cross-sections of CORA 5 show two blockages. One is caused in the lower part of the bundle by molten (Ag,In,Cd) containing some Zr (Figure 34, lower picture). The other one is caused in the central region of the bundle by molten Zry containing dissolved UO_2 fuel (Figure 34, upper picture). The blockages formed according to the solidification temperatures of the melts at different axial temperature levels. The region in between the blockages exhibits less solidified melts [37,38]. Figure 35 shows details of the chemical interactions at the cross-section elevation 208 mm. CORA test 12 was terminated by quenching which resulted in a much stronger fragmentation of the bundle and an additional hydrogen generation [38].

The chemical interactions during the CORA tests could only be explained by the availability of the single effects test results. The resulting reaction products at room temperature can be understood, classified and the extent of interaction can be quantified. The results of the destructive post-test examinations of the CORA tests have been compared with TMI-2 core fragment and core bore examinations. Figure 36 shows as an example a comparison between the microstructure of the core bore specimen K9-P1/F and of the blockage region of CORA test 3. In both cases one can recognize regular UO_2 crystals grown in the metallic melt. The metallic phase within the UO_2 is metallic uranium which forms during cooldown as a result of the decomposition of hypostoichiometric UO_{2-x} into UO_2 and U. The UO_2 pellet columns are in both cases more or less intact and surrounded by metallic once molten material of different chemical compositions.

In the bundles with Al_2O_3 pellets (burnable poison rods) early melt formation starts at about 1350 °C and increases remarkably after reaching 1500 °C (see chapter 6.1). The formation of a metallic (Zr,Al,O) alloy is important in this process. From the refrozen material one can distinguish three different types of once molten material: a metallic (Zr,Al,O) alloy, metallic molten Zry of different

oxygen content and a ceramic (ZrO_2/Al_2O_3) mixture. The (Zr,Al,O) alloy can be liquid already at about 1350 °C, the oxygen-poor Zry will melt above 1760 °C and the ceramic Al_2O_3/ZrO_2 and Al_2O_3/ZrO_2 eutectics will be liquid above about 1850 °C [32]. The melt formation from burnable poison rod failure will result in strong additional fuel liquefaction in the burnable poison rod fuel assemblies.

8. Core-Melt Progression Phenomenology

In-vessel core-melt progression should be divided into so-called unmitigated and mitigated degraded core accidents. A few of the material relocation processes will be different or can even be avoided in mitigated accident scenarios. However, since this depends strongly on the individual accident sequence a more general description of the material behavior in the core with increasing temperature will be given. This reflects the current status of knowledge in this area.

The in-pile experiments performed in the PBF, ACRR, NRU and LOFT reactors and the out-of-pile experiments performed in the NIELS and CORA facilities as well as many single-effects tests have shown that many competing chemical interactions and material relocation processes can take place in the reactor core with increasing temperature under core-uncovering accident conditions. Some of these processes have been identified in TMI-2 core examinations. The oxidation of Zircaloy cladding and stainless steel are important factors, because of: 1) the metallurgical implications; 2) the heat generated by these processes; and 3) the loss of core geometry due to run-off of molten materials and reaction products and the related mechanical collapse of portions of the core into these slumped regions. Local and/or large-scale blockages in the lower regions of the core formed due to resolidification of the molten material can cause subsequent heat up, because cooling still can be inadequate, causing further melt progression and material relocation into lower regions of the reactor vessel.

Another phenomenon is the formation of rubble beds. The collapse of solid material onto the blockages (solidified materials and grid spacers) can form debris beds on top of the blockages. Continuous heatup of these debris beds can form molten pools, held in place by a solid crust, which acts as a crucible (as

evidenced by TMI-2), with later crust collapse possibly influencing the late-melt relocation stage.

The presence of water and/or the injection of water due to safety devices or operator iactions have an important effect on the in-vessel core-melt progression. For example, if emergency core cooling water enters the reactor vessel early during the melt-down process (early reflood) there will be only limited fragmentation and collapse of solid but embrittled material. The longer the delay in establishing this water flow (late reflood), the greater will be the amount of both molten and embrittled materials. Ultimately, in-core configurations could be formed that are not coolable in place. This is thought to have caused the collapse of molten material into the RPV lower head in TMI-2. During the process of melt relocation the grid structures can provide a major impediment to the downward movement of melts.

8.1 Temperature regimes for liquid phase formations

There exist three distinct temperature regimes in which liquid phases can form in large quantities, either due to primarily eutectic chemical interactions or by reaching a melting point (range). These are as follows (Figure 37):

a) At temperatures between 1200 and 1400 °C the Ag,In,Cd control rods possibly may start to fail directly as a result of chemical interactions between the stainless steel cladding of the absorber rods and the Zircaloy guide tube or by simple mechanical rupture of the cladding (low system pressure case). However, in some situations, failure could be delayed until stainless steel melting at about 1400 °C (high system pressure case). The failed absorber rod releases the liquid (Ag, In, Cd) alloy, which melts at about 800 °C . This alloy interacts eutectically with Zircaloy, but not with stainless steel, and can liquefy the Zircaloy much below its melting point ($\approx$ 1760 °C). This would enable the damage to propagate to neighbouring Zircaloy-clad fuel pins. The associated liquefaction and relocation can open axial and radial flow pathways through the whole core. Since the solidification temperatures of these material mixtures are extremely low they should reach first the lower core structures. Or they may fall into the water below the core, and ultimately into in the lower head of the RPV and cause additional steam generation which may temporarily overcome steam starvation in some of the upper portions of the core. Due to the low-temperature failure of the control rods and fast relocation to colder parts of the core the Cd vaporization will be strongly reduced.

   Other low-temperature eutectic interactions can occur between the Zircaloy of the guide tube and Inconel of the spacer grids. At about 1400 °C

these interactions result in a localized failure of the fuel rods, the formation of molten phases and the relocation of liquefied Zircaloy cladding material far below its melting point. This type of fuel rod failure mode causes early fission product release in a high-pressure accident scenario. In a low-pressure accident scenario the cladding will balloon and rupture at even much lower temperatures.

b) Between 1800 and 2000 °C, the unoxidized portions of the Zircaloy cladding of the fuel rods, which are still metallic, start to melt and can chemically dissolve the solid UO_2 fuel and the ZrO_2 surface sheath that oxidation is producing on the cladding OD. The amount of unoxidized cladding depends on heatup rate and steam availability. The molten metallic Zircaloy then relocates downwards along the individual rods in a slow "candling process" or by a fast "dropping" process and is so removed from the higher-temperature regions of the core where quicker oxidation prevails. These processes can notably limit the uncontrolled temperature escalation and the corresponding rapid hydrogen generation caused by Zircaloy oxidation.
Molten metallic Zircaloy can chemically dissolve large quantities of solid UO_2 fuel and "liquefy" it at about 1800 °C, around 1000 °C below the melting point of UO_2 ($\approx$ 2850 °C). Due to this liquefaction process of the oxide fuel, starting at about 1800 °C, low-temperature melt relocation of (Zr,U,O) mixtures, containing decay heat sources, will take place. This relocation is also part of the so-called candling process. Solidification and melting will occur in a repetitive way as water boils off and core-melt progression proceeds. At the same time molten metallic Zircaloy can chemically dissolve ZrO_2 too and breach the ZrO_2 shell on the cladding surfaces.

If burnable ($Al_2O_3 + B_4C$) poison rods are present further low-temperature liquid phases can form already below 1800 °C. Around 1850 °C eutectic interaction will commence as soon as alumina comes into contact with either the ZrO_2 on the oxidized cladding surface or with UO_2. The possible influence of burnable poison rods is emerging from TMI-2 examinations (see chapter 6).

c) In regions of the core where temperatures between 2600 and 2850 °C may be reached the $(U,Zr)O_2$ solid solution, which may form in the fuel pin during a slow core heat-up or may form as a result of UO_2 dissolution by molten Zry, starts to melt and relocate. At temperatures above 2850 °C all components of the reactor core and chemically formed phases will be molten, including UO_2 itself which has the highest melting point ($\approx$ 2850 °C). The melting point of ZrO_2 is about 2700 °C.

The different temperature regimes result in different core damages. Regime a) causes localized core damage and the formed blockages will be probably coolable. In the temperature regime b) much stronger melt formation occurs with extended core damage and the generation of core regions which cannot be cooled anymore. Regime c) finally results in the complete meltdown of all materials and a total destruction of these high-temperature core regions.

Evidence for all these molten phases and relocation processes have been seen in the various in-pile and out-of-pile experiments and in TMI-2. The various molten phases will solidify on cooldown at different temperatures and may therefore form blockages at different axial locations, although the undestroyed spacer grids may define the limit of axial slumping. It is not yet clarified to what extent the flow channel blockages affect the boil-off steam flow rate and as a consequence the Zircaloy oxidation and hydrogen generation, although the disruption of core geometry and flow paths caused by the core slumping probably would decrease Zircaloy oxidation efficiency within the core.

8.2 Influence of heat-up rates

Not only the temperature of the core, but also the local heat-up rates have an important influence on the in-vessel core-melt progression. These local heat-up rates can be largely controlled by local steam availability because of the importance of the exothermic Zircaloy/ steam reaction. At initial slow heat-up rates below 0.5 K/s the fuel cladding will be completely oxidized to ZrO_2 under steam-rich conditions before reaching the melting point of metallic Zircaloy. As a result fuel rod melting will not occur until 2600 °C. At initial heat-up rates above 1 K/s temperatures are reached which permit the Zircaloy metal to melt and dissolve UO_2 before all the Zircaloy becomes oxidized. The melt may not relocate because it can be held in place by the solid ZrO_2 layer that has been formed during heat-up on the surface of the Zircaloy cladding. Zircaloy oxidation may be also limited by steam starvation. At fast heat-up rates above 5 K/s, the ZrO_2 layer will probably be too thin to hold the metallic melt in place and relocation will occur after mechanical and/or chemical breach of the ZrO_2 shell.

It is evident from the foregoing discussion that the in-vessel melt progression process is very complex. It can only be understood by a combination of experiments and computer modeling, and careful verification and validation of such codes. The latter activity requires careful and thorough analysis of the out-of-pile and in-pile tests, the large-sized LOFT-FP2 experiment, and the TMI-2 accident. Both TMI-2 and LOFT-FP2 can be linked to smaller-scale separate effects tests to look at particular phenomena. The computer models, when validated against these smaller-scale experiments must allow application to reactor plant conditions where scaling effects become important.

9. Discussion

Elevated core temperatures cause a variety of physical and chemical changes in the various core components like the UO_2 fuel, the Zry cladding, the Inconel spacer grid, the stainless steel clad (Ag,In,Cd) absorber rod, the Al_2O_3-containing burnable poison rod and the stainless steel structural materials, resulting in typical metallographic structures of the components and of the reaction products. These phenomena include grain growth, phase transformations, type and extent of chemical interactions, formation of precipitates, melting of the components or reaction products, UO_2 and/or ZrO_2 dissolution, and the solidification of the melts. Since most of these phenomena leave characteristic patterns in the resulting microstructures of the various phases, these microstructures can be compared with those obtained in well defined out-of-pile annealing or interaction experiments described above. The microstructure is therefore one important tool in the identification of the chemical interactions. Another tool is the chemical analysis of the specimens by SEM/EDX, SEM/WDX or other methods. The analytical results can then be used, together with available phase diagram information, to make statements concerning the interactions, the formation of liquid phases and peak temperatures. However, in most cases only the equilibrium phase diagrams of very simple binary or ternary systems are known, which can only be applied to a limited extent for the complex multi-component core system.

It is particularly important to emphasize that many complex phenomena occur simultaneously or in series during a severe accident, due to large variations in individual rod temperatures and local steam flow rates, and also because of the relocation of absorber rod material, cladding, and fuel. The resultant solid and liquid phases encompass a wide range of initial and final chemical compositions. However, what can be identified through post-test metallographic and analytical examinations at room temperature indicates only the chemical and physical state of the reaction products that were present when cooldown or quenching of the fuel rod bundle or core region occurred. Only in a few cases, the time-dependent material behaviour during the accident scenario may be postulated.

It is also important to keep in mind the fact that the microstructure (number of phases) of the components of reaction products at room temperature may be different than that which exists under the physical and chemical conditions at

test temperature or during a severe accident. A microstructure that is multiphase at room temperature may have been single-phase at high temperatures. This can have an influence on some physical properties, such as the meltdown behaviour of liquid phases determined by the wetting properties between the melt and the solid substrate. Furthermore, as a result of the fast cooldown rate, the phases may not be under equilibium conditions. For this reason, the application of available phase equilibrium diagram information is limited.

As a result, the complexity of a severe reactor accident scenario and the resulting multitude of materials interactions make a complete interpretation of the many possible chemical interactions extremely difficult and in some cases even impossible. However, it will be possible to indicate to a large extent the temperatures at which liquid phases will form and may relocate and solidify.

The various temperature regimes indicated provide a basis for possible accident management measures to stop the severe reactor accident transient even within the reactor pressure vessel.

Summary and Conclusions

In a large variety of single effects tests and out-of-pile and in-pile tests it was shown that the chemical interactions between the various reactor core components, which result in the formation of liquid phases, can be classified in three distinct temperature regimes: a) 1200 - 1400 °C, b) 1800 - 2000 °C and c) 2600 - 2850 °C.

First reactios start to become important approaching 1200 °C. At this temperature the uncontrolled temperature escalation of the fuel rod cladding starts due to the exothermal Zry/steam interaction with a rapid heatup of the fuel rods to about 2000 °C, provided that there is enough steam available.

Above 1200 °C a liquefaction of portions of the absorber rod fuel assemblies occurs as a result of Zry/stainless steel and Zry/(Ag,In,Cd) interactions. The low-temperature melt of (Ag,In,Cd) absorber rod material will relocate and form coolant channel blockages on solidification in the lower part of the fuel rod bundle.

Above 1400 °C the absorber rods and the Inconel spacer grids will be completely molten. The resulting metallic melt is able to dissolve the Zry cladding of the fuel rods and the UO_2 fuel far below their melting points. The kinetics of the fuel dissolution accelerates after the onset of melting of the unreacted metallic Zry cladding, e.g. above about 1800 °C.

There are always competitive interactions between the various metallic core components among each other, with the UO_2 fuel and with the available steam. The final thermodynamically stable reaction products in the core are oxide compounds, with the exception of Ag of the absorber rod. Even in the case of metallic eutectic phase formation, the resulting melts will be oxidized later in the course of a severe accident. It may also happen that metallic melts reach core regions where further interaction will not continue due to the low temperatures.

As a result of the multi-component interaction and phase formation the onset of melting of the oxide mixture will be shifted to lower temperatures. Therefore, the various oxidized core components and the resulting mixture will be completely liquefied at about 2600 °C. This was probably the case in the TMI-2 accident. The oxidic melt, which relocated from the core region into the lower RPV head, contained besides U, Zr, O, various amounts of the stainless steel components, Al and other minor constituents.

Depending on the chemical composition and oxidation state of the various core materials the completely molten components and phases will form in the high-temperature regime 2600 - 2850 °C either a homogeneous metallic or homogeneous ceramic melt or two immiscible melts. The solidification temperatures of both types of melts can vary in a rather large range. The onset of solidification for the ceramic melt will be distinctively higher compared to that of the metallic melt. The solidification temperature for the ceramic melt will be at about 2400 °C and that for the metallic melt at about 1800 °C. In both cases, the temperature range for complete solidification of the melts can be very wide.

The present knowledge provides a better understanding of the physical and chemical processes contributing to the degradation of a reactor core with increasing temperature and provides a reasonable basis for code development and verification.

Acknowledgement

We would like to thank Dr. C.M. Allison (EG + G Idaho), Prof. Dr. W. Dienst (KfK) and Dr. R.R. Hobbins (EG + G Idaho) for thorough technical and editorial reviews of the manuscript.

References

[1] H. M. Chung, G.R. Thomas, The Retarding Effect of Hydrogen on Zircaloy Oxidation. NSAC-29, (1981)

[2] S. Leistikow, G. Schanz, H. v. Berg, A.E. Aly, Comprehensive Presentation of Extended Zircaloy-4 Steam Oxidation Results (600 - 1600 °C). Proc. OECD/IAEA Specialists' Meeting, Risø, Denmark, (1983), IWGFPT/16, 188 - 199

[3] J.T. Prater, E.L. Courtright, High-Temperature Oxidation of Zircaloy-4 in Steam and Steam-Hydrogen Environments. NUREG/CR-4476, PNL-5558, (1986)

[4] S. Leistikow, G. Schanz, Oxidation Kinetics and Related Phenomena of Zircaloy-4 Fuel Cladding Exposed to High Temperature Steam and Steam-Hydrogen Mixtures Under PWR Accident Conditions. Nucl. Engin. Des., 103 (1987) 65 - 84

[5] H. Uetsuka, T. Otomo, S. Kawasaki, Oxidation of Zircaloy-4 Funder Limited Steam Supply from 1000 to 1400 °C. J. Nucl. Sci. Technol., 23 (1986) 928 - 930

[6] P. Hofmann, H.J. Neitzel, Experimental and Theoretical Results of Cladding Oxidation Under Severe Fuel Damage Conditions. Seventh International Conference on Zirconium in the Nuclear Industry, Strasbourg, France, (1985), ASTM-STP 939, 504-538

[7] F.J. Erbacher, S. Leistikow, A Review of Zircaloy Fuel Cladding Behavior in a Loss-of-Coolant Accident, KfK 3973, (1985)

[8] H.M. Chung, T.F. Kassner, Embrittlement Criteria for Zircaloy Fuel Cladding applicable to Accident Situations in Light-Water-Reactors. Summary Report. NUREG/CR-1344, (1980)

[9] S. Leistikow, G. Schanz, Z. Zurek, Comparison of High Temperature Steam Oxidation Behavior of Zircaloy-4 versus Austenitic and Ferritic Steels under Light Water Reactor Safety Aspects. KfK 3994, (1985)

[10] C. Petersen, G. Schanz, S. Leistikow, High Temperature Behavior of CrNi-Steel DIN Material No. 1.4970 Cladding Materials in Respect to Advanced Pressurized Water Reactor Safety Considerations. Nuclear Technology 80, (Jan 1988) 161 - 172

[11] P. Hofmann, D.K. Kerwin-Peck, UO_2/Zircaloy Chemical Interaction and Reaction Kinetics from 1000 to 1700 °C under Isothermal Conditions, KfK 3552 (1983)

[12] P. Hofmann, D.K. Kerwin-Peck, UO_2/Zircaloy Chemical Interactions under Isothermal Conditions and Transient Temperature Conditions, J. Nucl. Mater. 124 (1984) 80-105

[13] P. Hofmann, H.J. Neitzel, E.A: Garcia, Chemical Interaction of Zircaloy-4 Tubing with UO_2 Fuel and Oxygen at Temperatures between 900 and 2000 °C, KfK 4422 (1988)

[14] D.R. Olander, The UO_2/Zircaloy-Chemical Interactions, J. Nucl. Mater. 115 (1983) 271-285

[15] A. Denis, E.A: Garcia, A model to describe the interaction between UO_2 and Zircaloy in the temperature range from 1000 to 1700 °C, J. Nucl. Mater. 116 (1983) 44-54

[16] P. Hofmann, D.K. Kerwin-Peck, Chemical interactions of solid and liquid Zircaloy-4 with UO_2 under transient nonoxidizing conditions, Intern. Meeting on LWR Accident Evaluation, August 28-30 (1983), Cambridge, MA, USA

[17] P. Hofmann, H. Uetsuka, A.N. Wilhelm, E.A. Garcia, Dissolution of Solid UO_2 by Molten Zircaloy and its Modelling, Intern. Symp. on "Severe Accidents in Nuclear Power Plants", Sorrento, Italy, 21 - 25 March (1988)

[18] H.A. Saller et al., Phase Relations in the Uranium-Zirconium-Oxygen System Involving Zirconium and Uranium Dioxide, BMI 1023 (1955)

[19] C. Politis, Untersuchungen im Dreistoffsystem Uran-Zirkon-Sauerstoff, KfK 2167 (1975)

[20] A. Skokan, High-Temperature Phase Relations in the U-Zr-O System; 5th Int. Meeting on "Thermal Nuclear Reactor Safety", Sept. 9 - 13 (1984), Karlsruhe, FRG, KfK 3880/2B, 1035-42

[21] M. Miyake et al., Phase Diagram of the U-Zr-O System by Computer Calculation, 9th NSRR Technical Review Meeting, Nov. 20 - 22 (1985), Tokai, JAERI, Japan

[22] R.P. Elliot, Constitution of Binary Alloys, 1st Supplement, McGraw-Hill Book Co. (1965)

[23] R.J. Ackermann et al., The Lower Phase Boundary of ZrO_{2-x}, J. Am. Ceram. Soc. 61 (1978) 275-276

[24] R.F. Domagala and D.J. McPherson, The System Zirconium-Oxygen, Trans. AIME 200 (1954) 238-246

[25] E. Gebhardt et al., Untersuchungen im System Zirconium-Sauerstoff, Teil 2, J. Nucl. Mater. 4 (1961) 255-271

[26] R.J. Ackermann et al., High-Temperature Phase Diagram for the System Zr-O, J. Am. Ceram. Soc. 60 (1977) 341-345

[27] P. Hofmann et al., Constitution and Reaction Behavior of LWR-core Components at Core-Melting Conditions, KfK-2242 (1976)

[28] P. Nikolopoulos,P. Hofmann, D.K. Kerwin-Peck, Determination of the interfacial energy and work of adhesion in the UO_2/Zircaloy-4 diffusion couple, J. Nucl. Mater. 124 (1984) 106-113

[29] K.T. Kim, D.R. Olander, Dissolution of UO_2 by Molten Zircaloy, J. Nucl. Mater. 154 (1988) 85-115

[30] Proceedings of the First International Information Meeting on the TMI-2 Accident, October 21 (1985), Germantown, MD, CONF-8510166

[31] P. Hofmann, M. Markiewicz, J.L. Spino, Chemical Interaction between Al_2O_3, which is used in Burnable Poison Rods, and Zircaloy-4 up to 1500 °C, to be published in J. Nucl. Mater. (1989)

[32] S. Hagen, P. Hofmann, G. Schanz, L. Sepold, Interaction between Al_2O_3 Pellets and Zircaloy Tubes in Steam Atmosphere (Results from the CORA Tests B and C), KfK 4313 (1988)

[33] P. Hofmann et al., Reaktionen in LWR-Brennelementen bei sehr hohen Temperaturen, KfK 4450 (1988) 36-62

[34] S. Hagen, P. Hofmann, Physical and Chemical Behaviour of LWR Fuel Elements up to very High Temperatures, KfK 4104 (1987)

[35] S. Hagen, P. Hofmann, G. Schanz, L. Sepold, Results of the Severe Fuel Damage Experiments CORA-2 and CORA-3, KfK 4378 (1989)

[36] S. Hagen, P. Hofmann, G. Schanz, L. Sepold, CORA Program, Int. Symp. on "Severe Accidents in Nuclear Power Plants", Sorrento, Italy, March 21 - 25 (1988)

[37] S. Hagen, P. Hofmann, G. Schanz, L. Sepold, Out-of-pile Experiments on the Meltdown Behaviour of LWR Fuel Elements, Int. ENS/ANS Conference on "Thermal Reactor Safety", October 2- 7 (1988) Avignon, France

[38] S. Hagen, P. Hofmann, G. Schanz, L. Sepold, Results of the CORA Tests 5 and 12, KfK 4419 (1989)

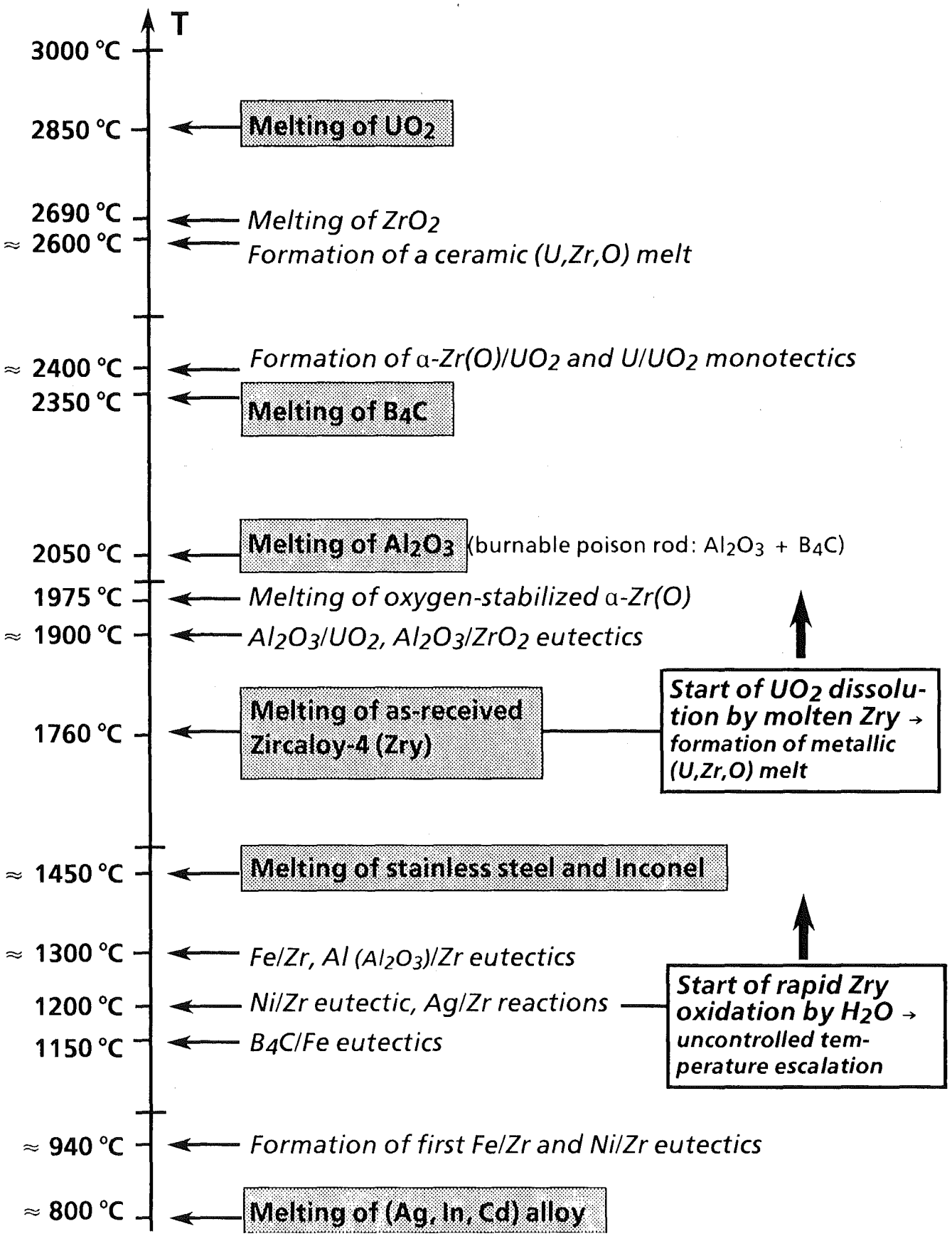

Fig. 1: Chemical interactions and formation of liquid phases in a LWR fuel rod bundle with increasing temperature.

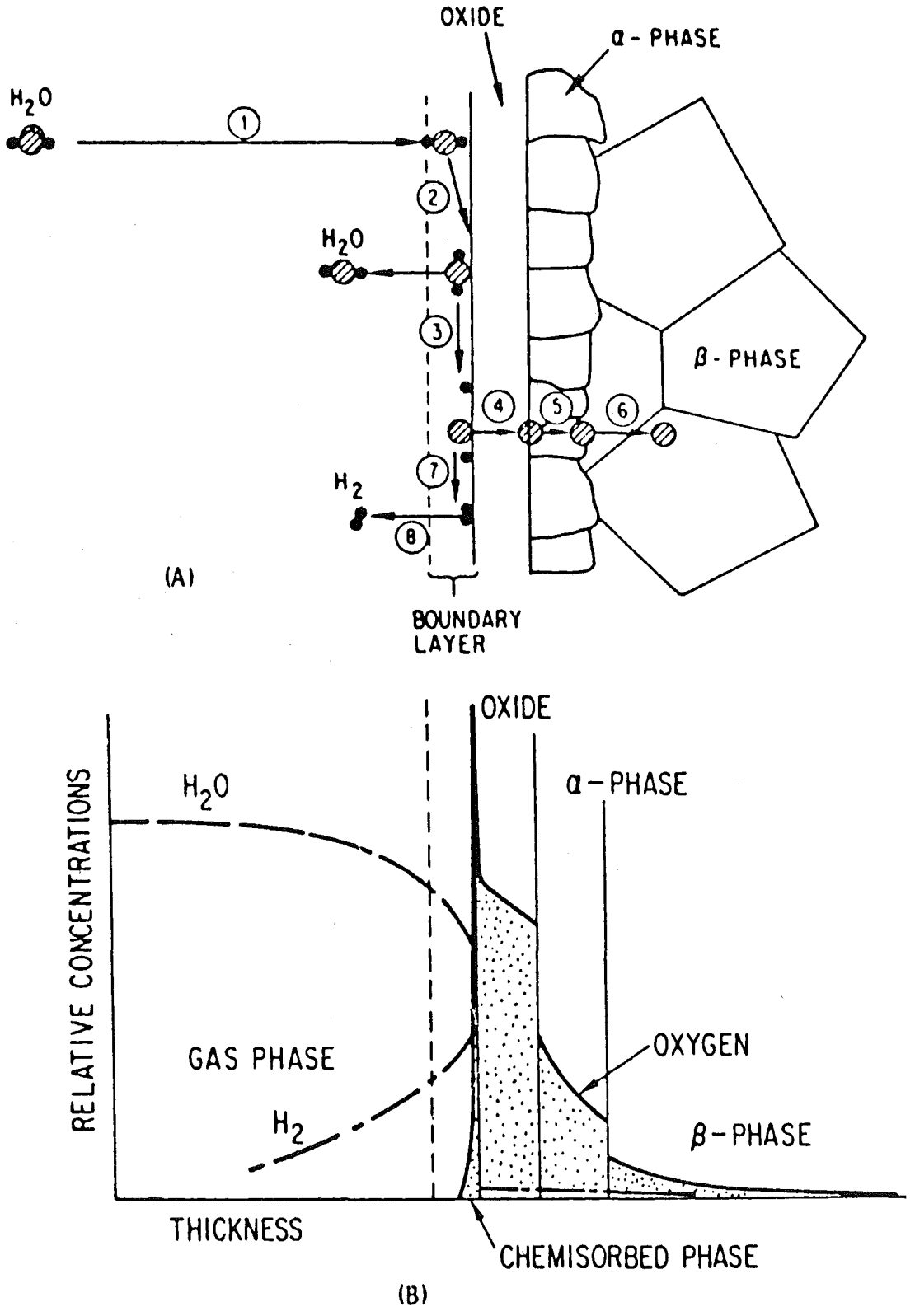

Fig. 2: Elementary mechanisms of Zircaloy-steam oxidation [1].
Schematic illustrations of (A) the physical processes during Zircaloy-steam oxidation and (B) the corresponding relative concentration gradients of reacting species across the phase layers. The elementary steps are gaseous diffusion of steam (1), chemisorption of steam (2), dissociation into oxygen and hydrogen (3), diffusion of oxygen in the oxide (4), alpha (5), and beta (6) phases, recombination of hydrogen (7), desoprtion of gaseous hydrogen (8).

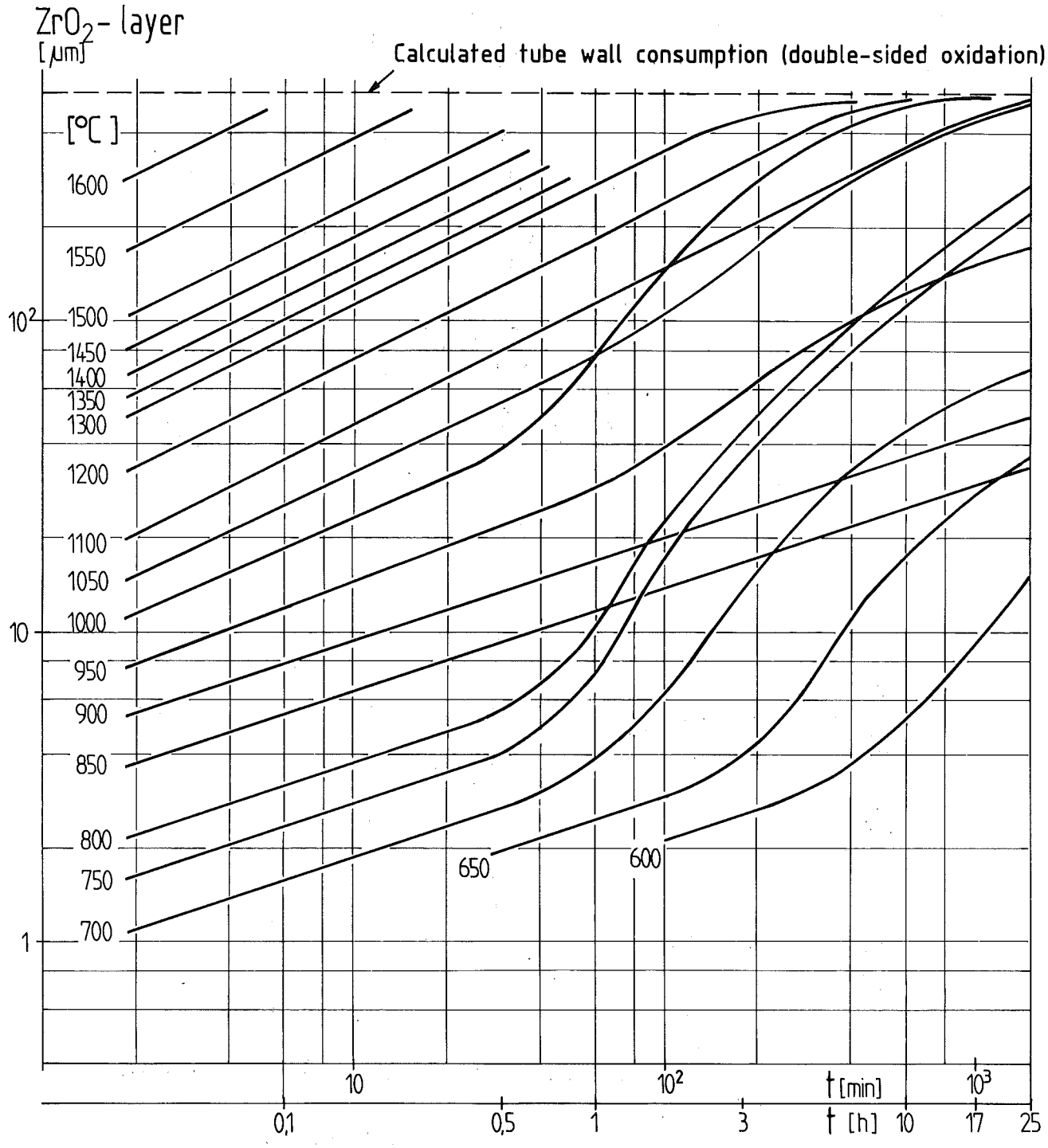

Fig. 3: High-temperature steam oxidation of Zircaloy-4 cladding. Kinetics of the ZrO_2 scale growth (600 - 1600 °C, 2 min - 25 h) [2].

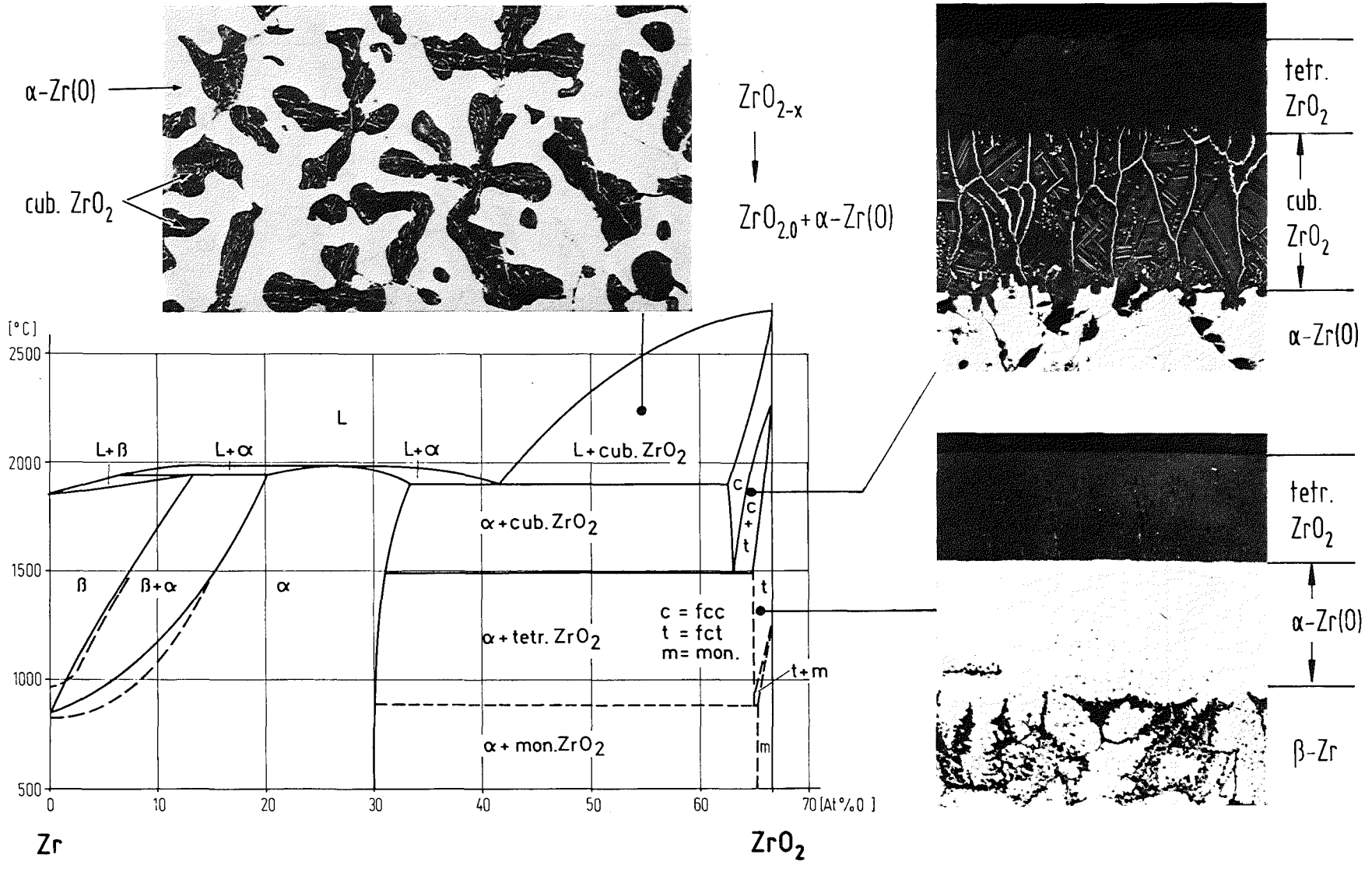

Fig. 4: Zirconium-oxygen phase equilibrium diagram [25].

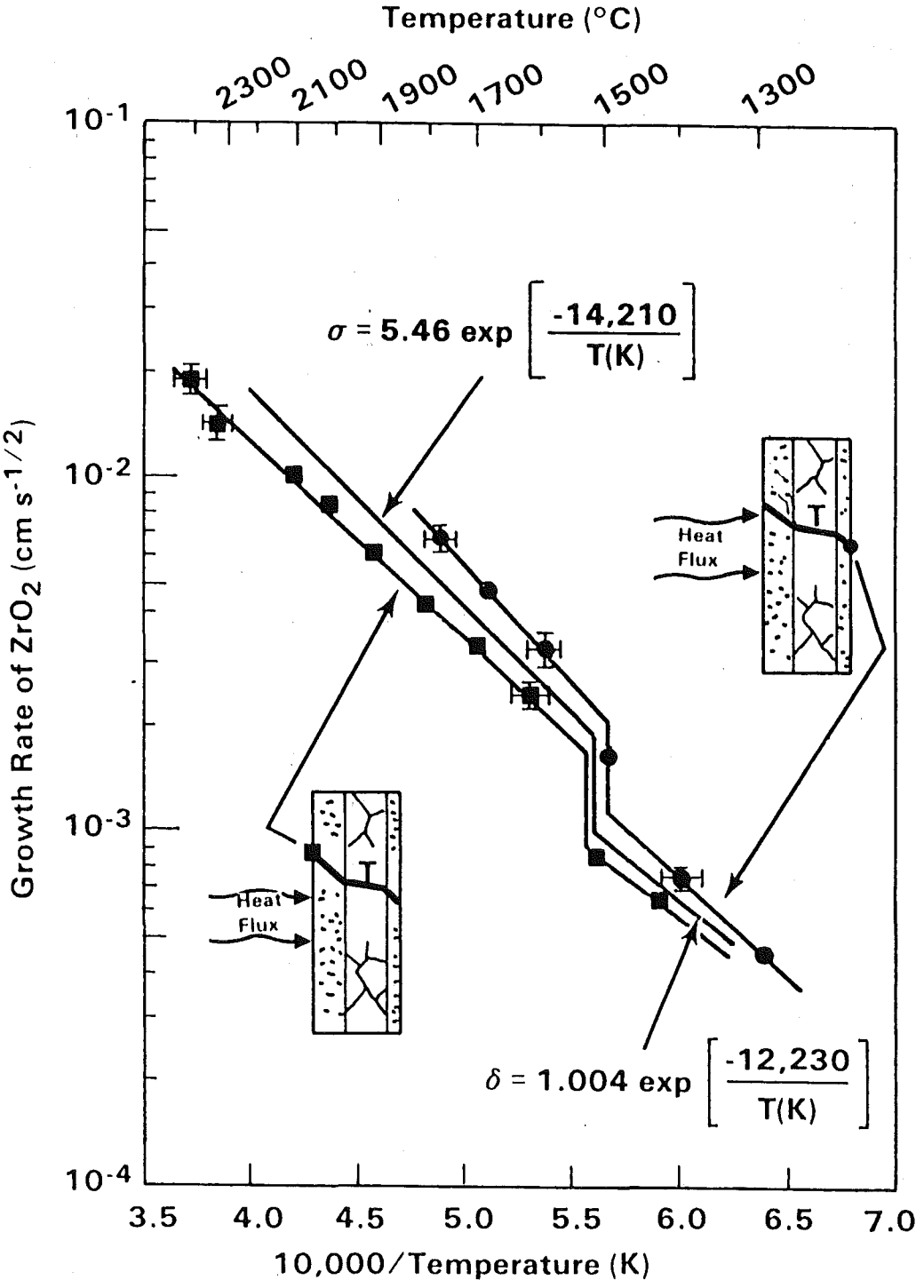

Fig. 5: Arrhenius plot of ZrO_2 scale growth rate [3].

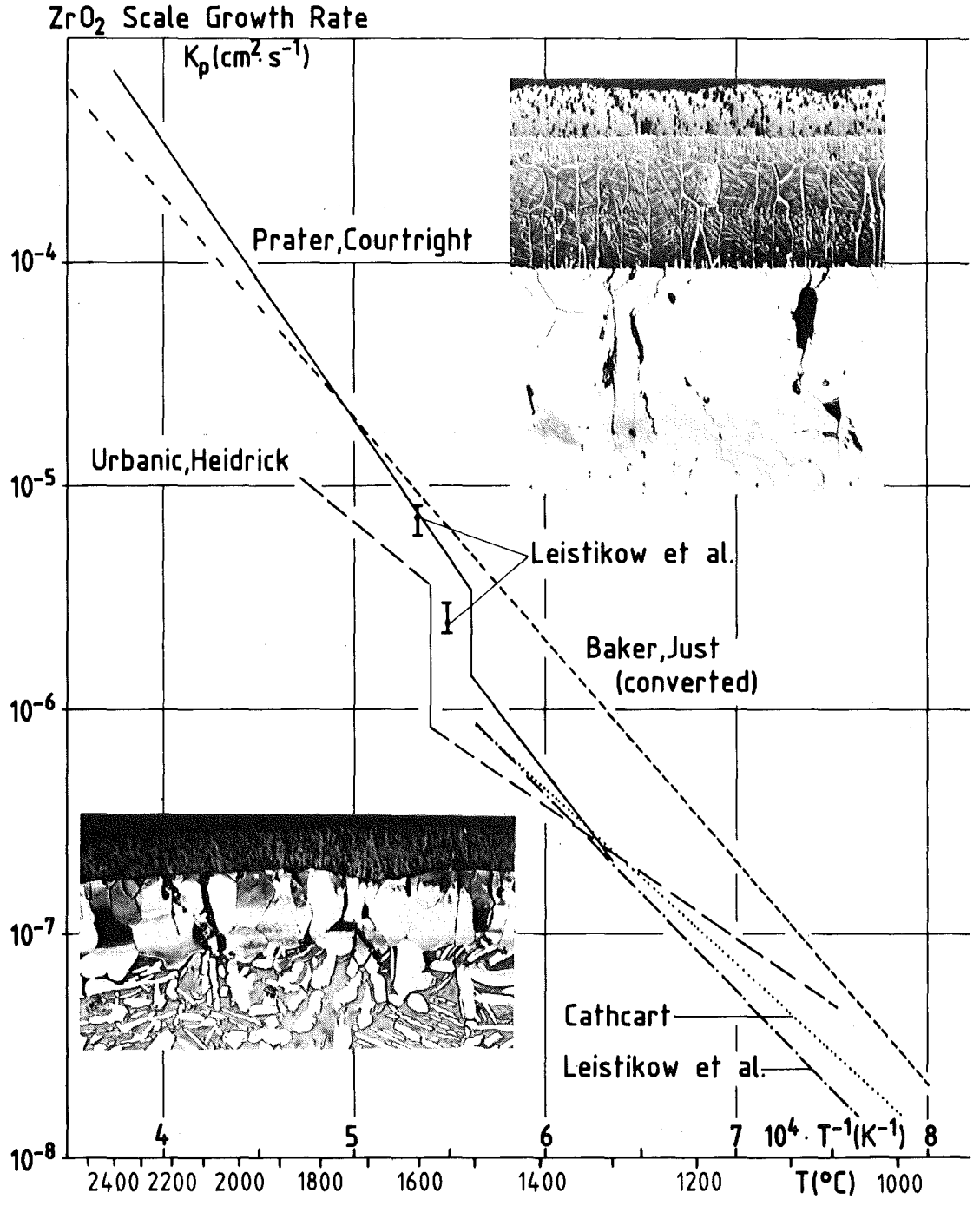

Fig. 6: Temperature dependence of parabolic growth rate of oxide scale formed on Zircaloy by oxidation in steam. Comparison of literature data [4].

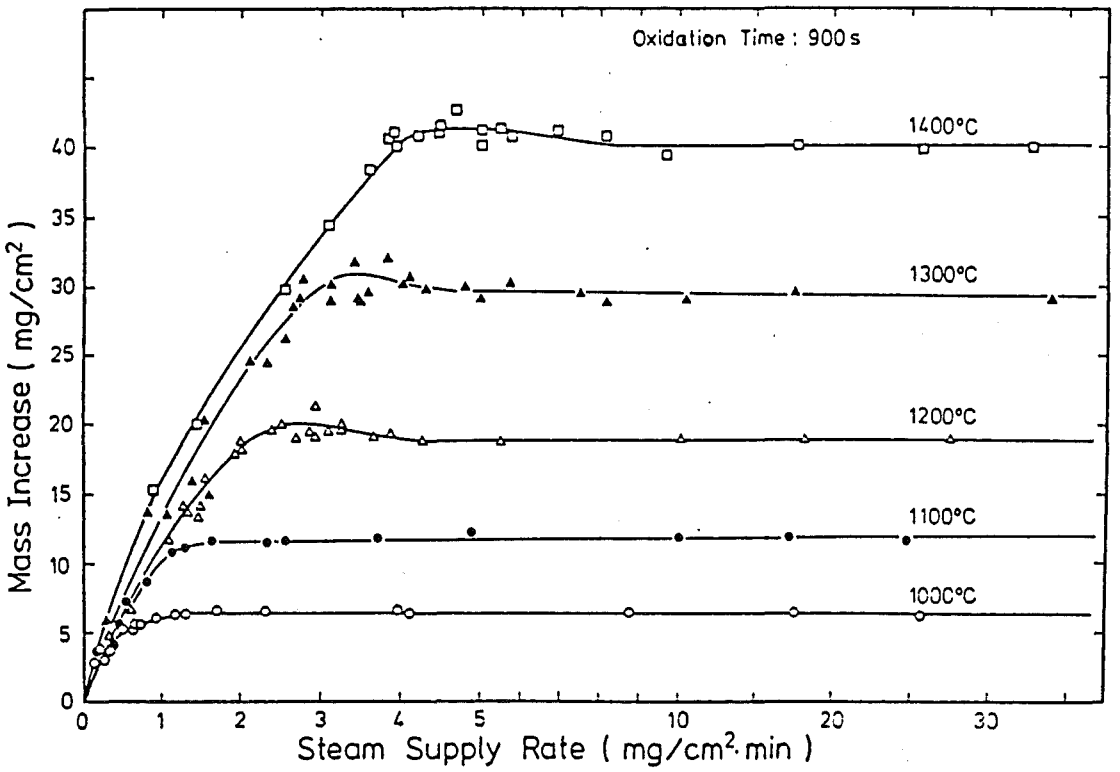

Fig. 7: Temperature dependence of the starvation limit of the steam supply rate [5].

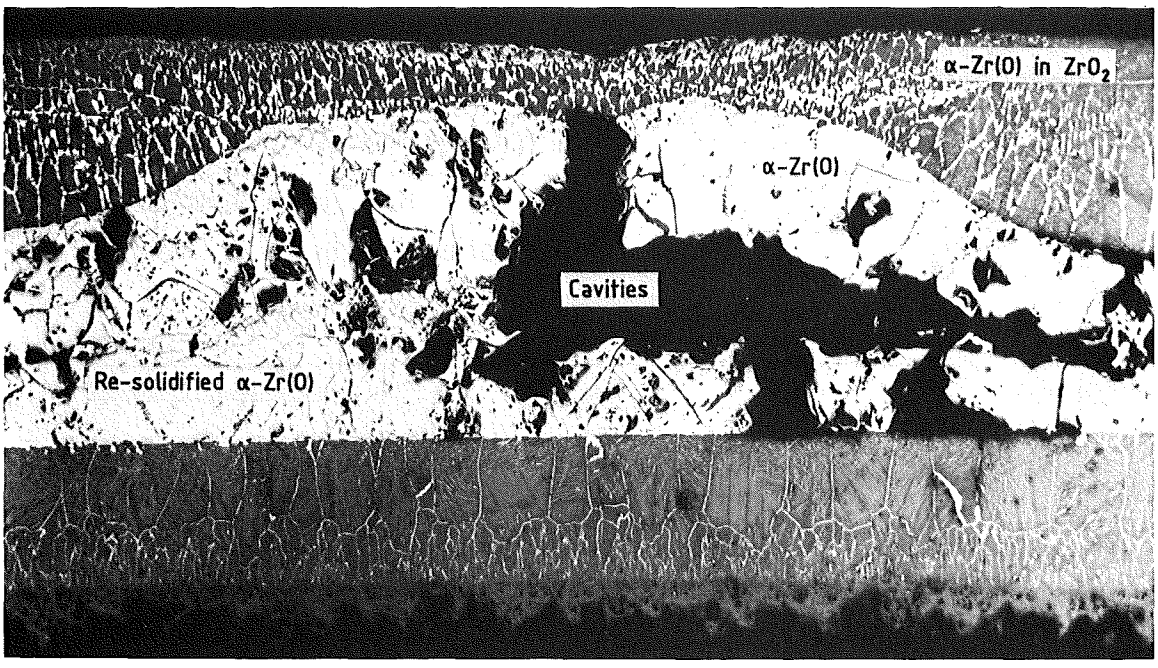

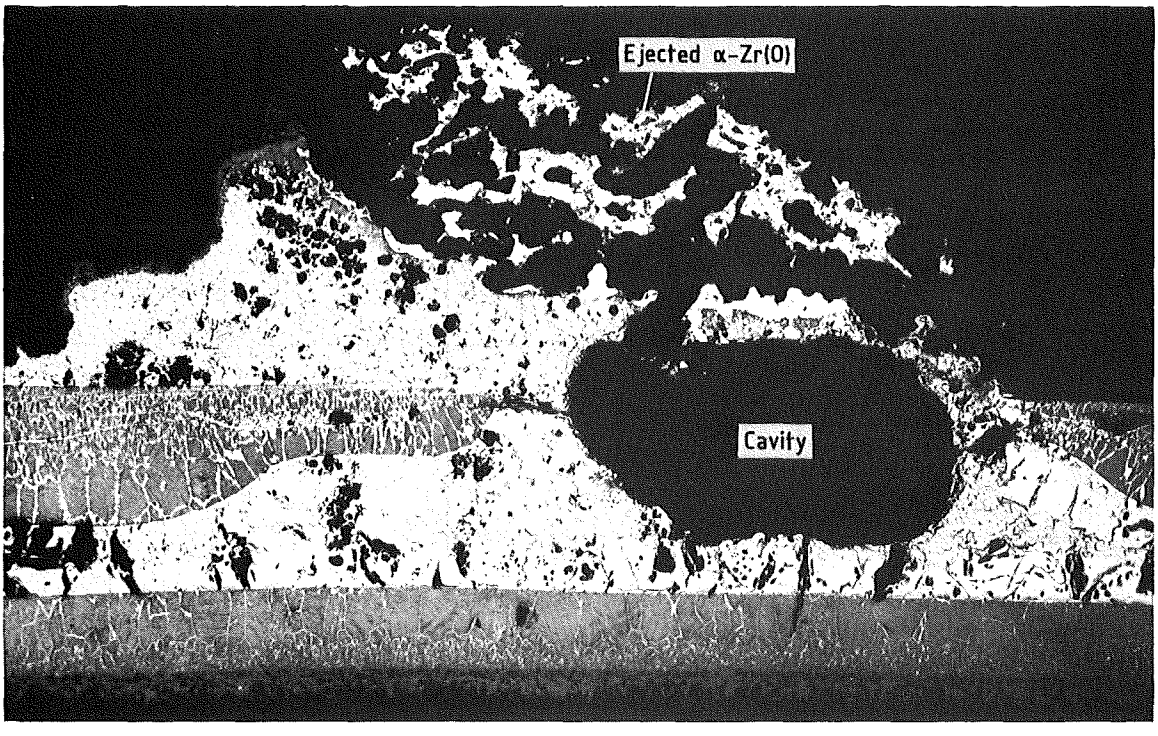

Fig. 8: Penetration of Zircaloy melt through dissolved ZrO_2 oxide scale.

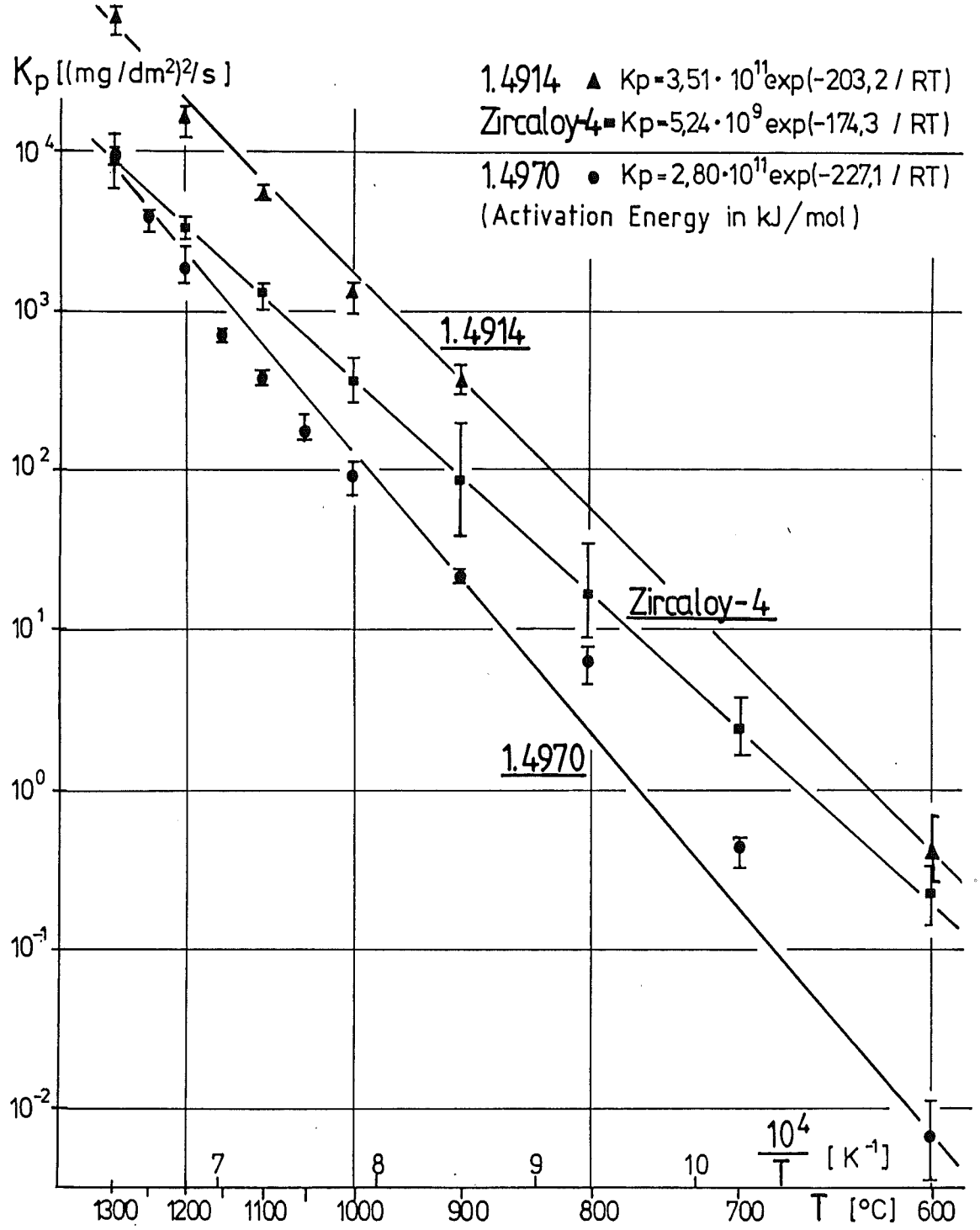

Fig. 9: Arrhenius diagram of mass increase by steam oxidation of ferritic-martensitic steel 1.4914 (X17CrMoVNb12 1), austenitic stainless steel 1.4970 (X10CrNiMoTiB15 5) and Zircaloy-4 (600 - 1300 °C, 6 h).

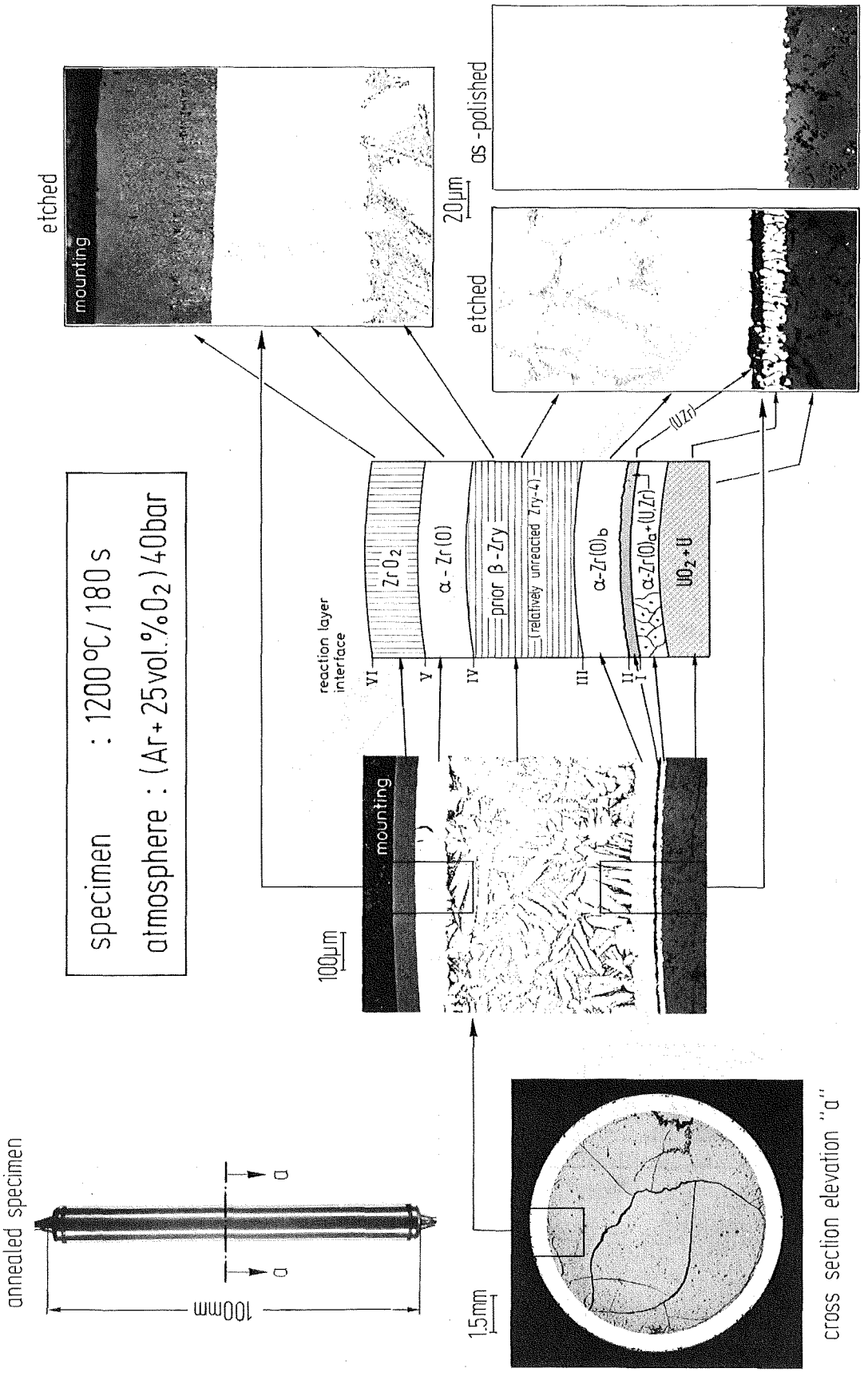

Fig. 10: Sequence of the external Zircaloy/oxygen and internal Zircaloy/UO_2 interaction layers.

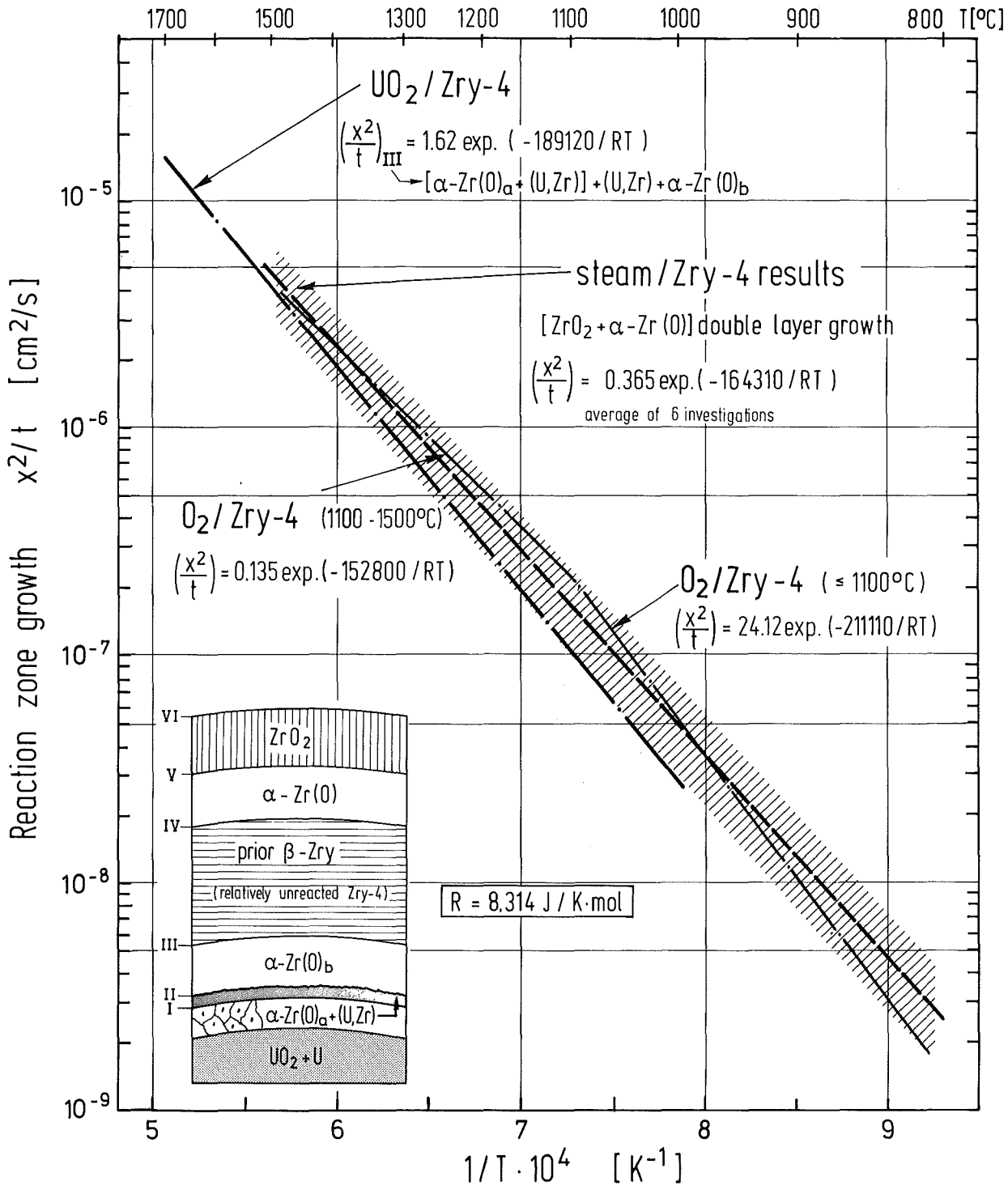

Fig. 11: Comparison of the growth rates for the Zircaloy/UO_2, Zircaloy/oxygen and Zircaloy/steam interactions.

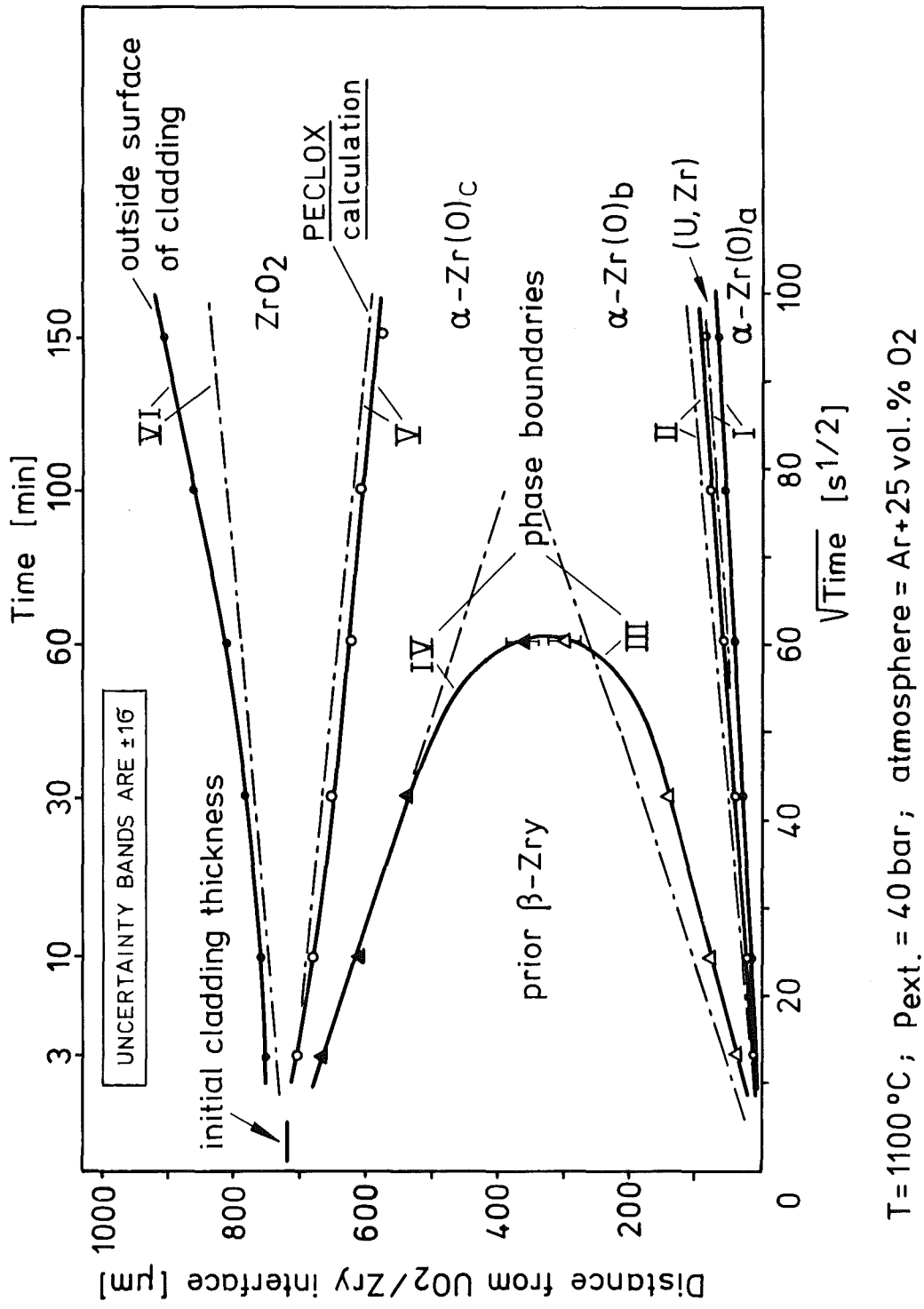

Fig. 12: Zircaloy/UO_2 and Zircaloy/oxygen reaction zone thicknesses versus the square root of time at 1100 °C. Comparison between experimental results and PECLOX calculation.

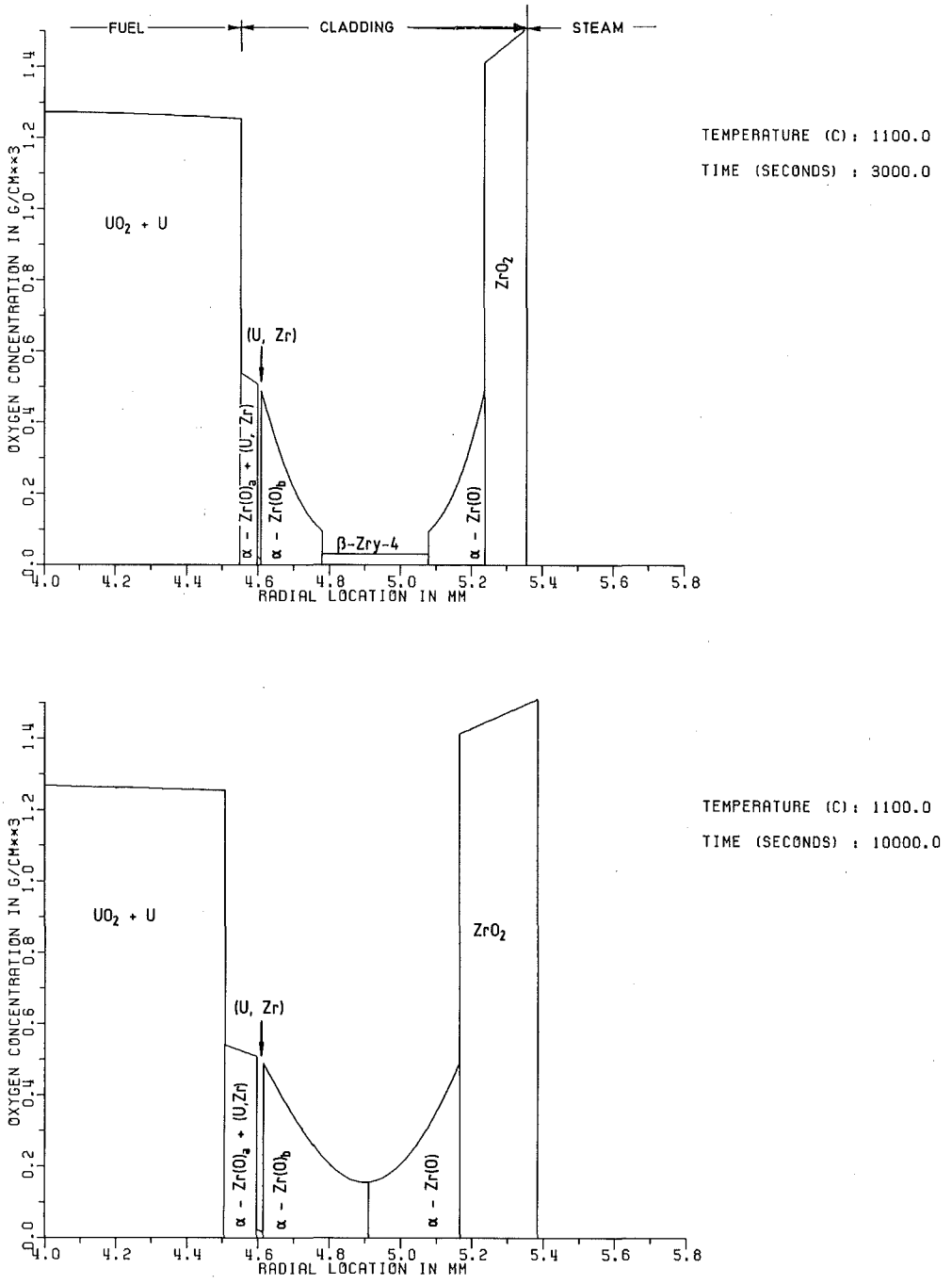

Fig. 13: Zircaloy/UO_2 and Zircaloy/oxygen interactions at 1100 °C. Oxygen concentration distribution in the various reaction layers after a) 3000 s and b) 10000 s reaction time.

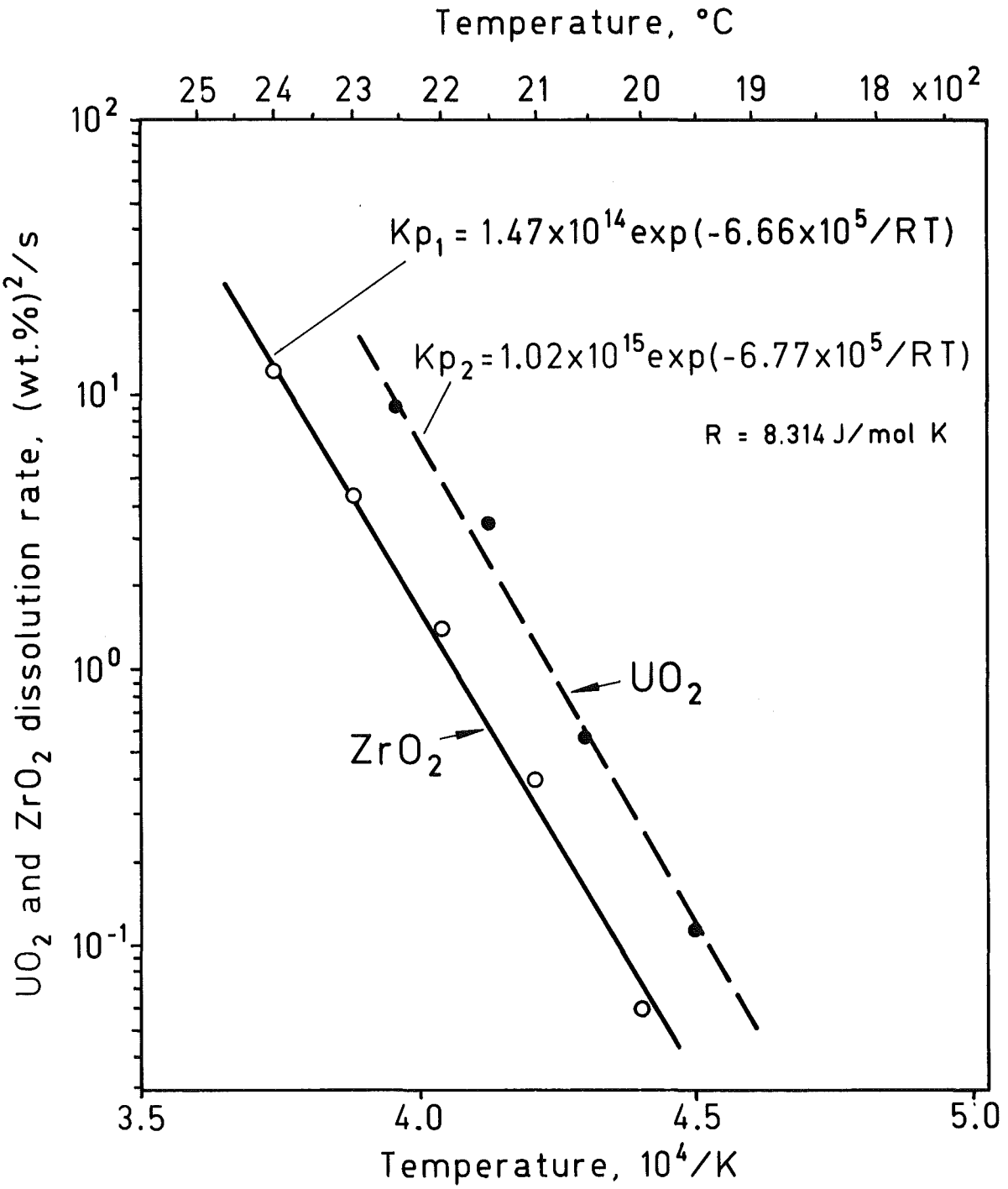

$$Kp = \frac{(wt.\% - a)^2}{t\ [s]} \longrightarrow (wt.\%)_{ZrO_2} = 23.3 + (Kp_1 \cdot t)^{0.5}$$

$$(wt.\%)_{UO_2} = 35.8 + (Kp_2 \cdot t)^{0.5}$$

Fig. 14: UO_2 and ZrO_2 dissolution rates by molten Zircaloy versus reciprocal temperature.

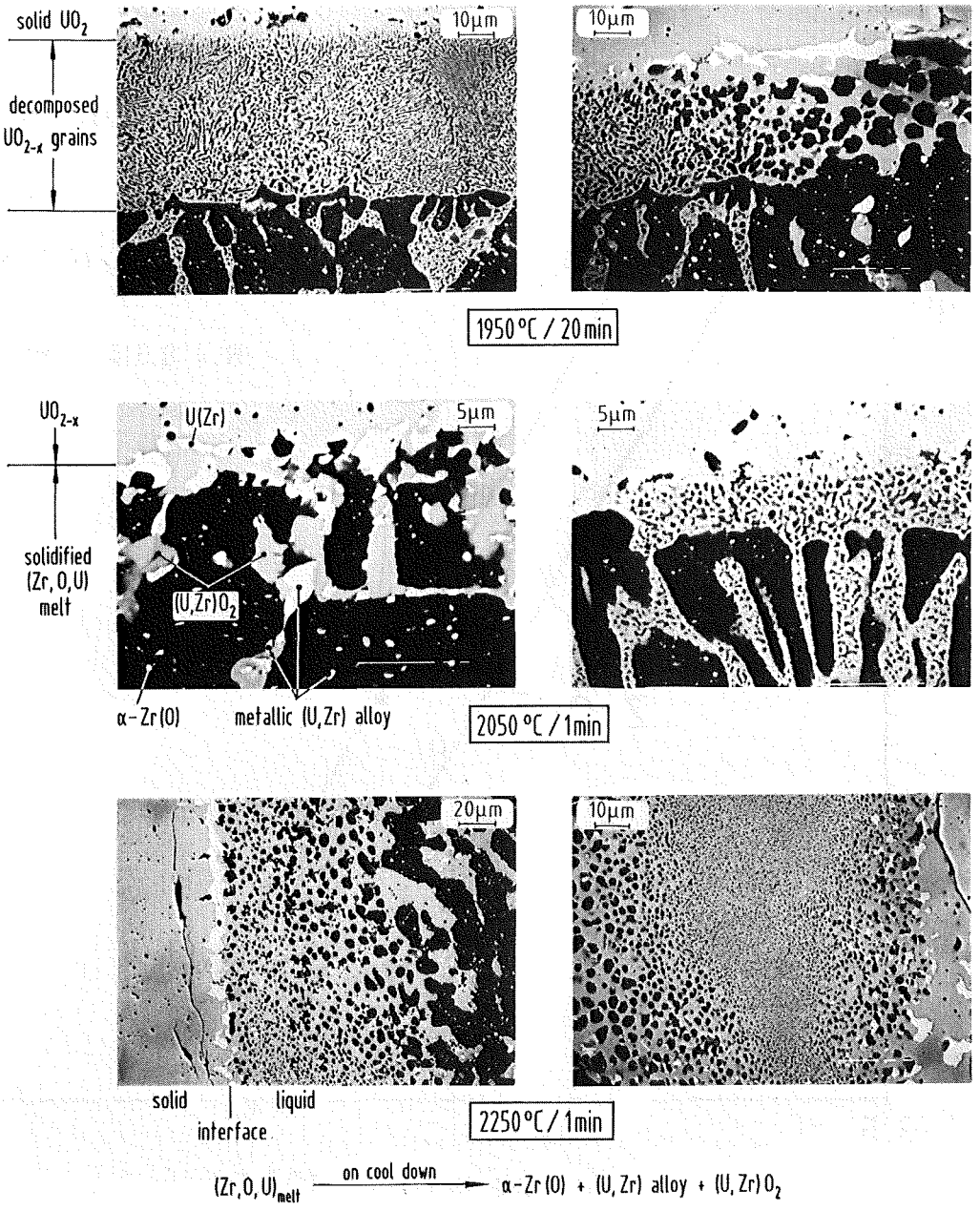

Fig. 15: Microstructure of the solid UO_2/molten Zircaloy interface. The fuel disintegrates in particles, partially much smaller than the original UO_2 grain size, which will be subsquently dissolved by the molten Zircaloy.

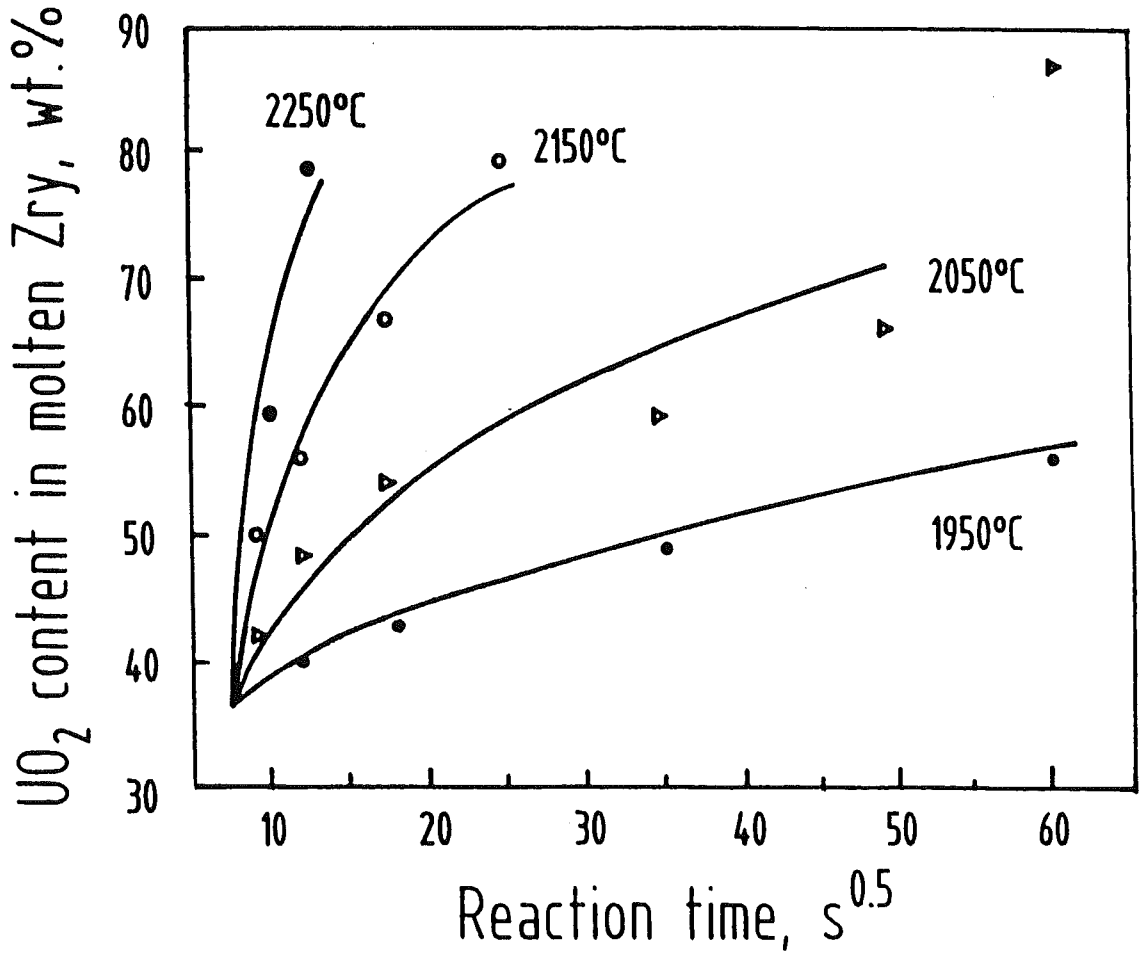

Fig. 16: Calculated values of the dissolved mass of UO_2 (in wt%) from numerical values of the UO_2/molten Zircaloy interface displacement obtained with the LISI code. The experimental data are superimposed [17].

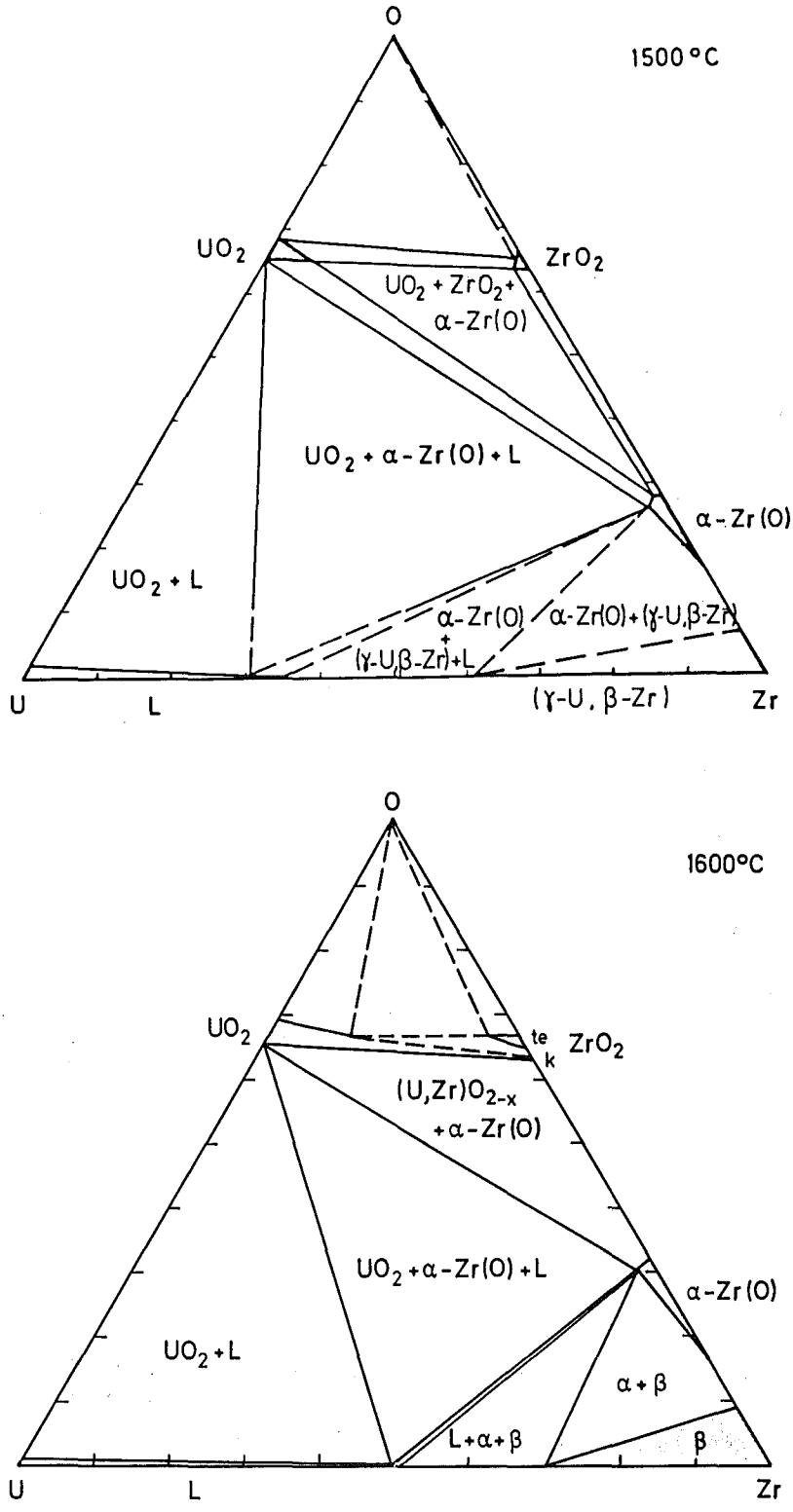

Fig. 17: Isothermal sections of the ternary U-Zr-O system at 1500 and 1600 °C.

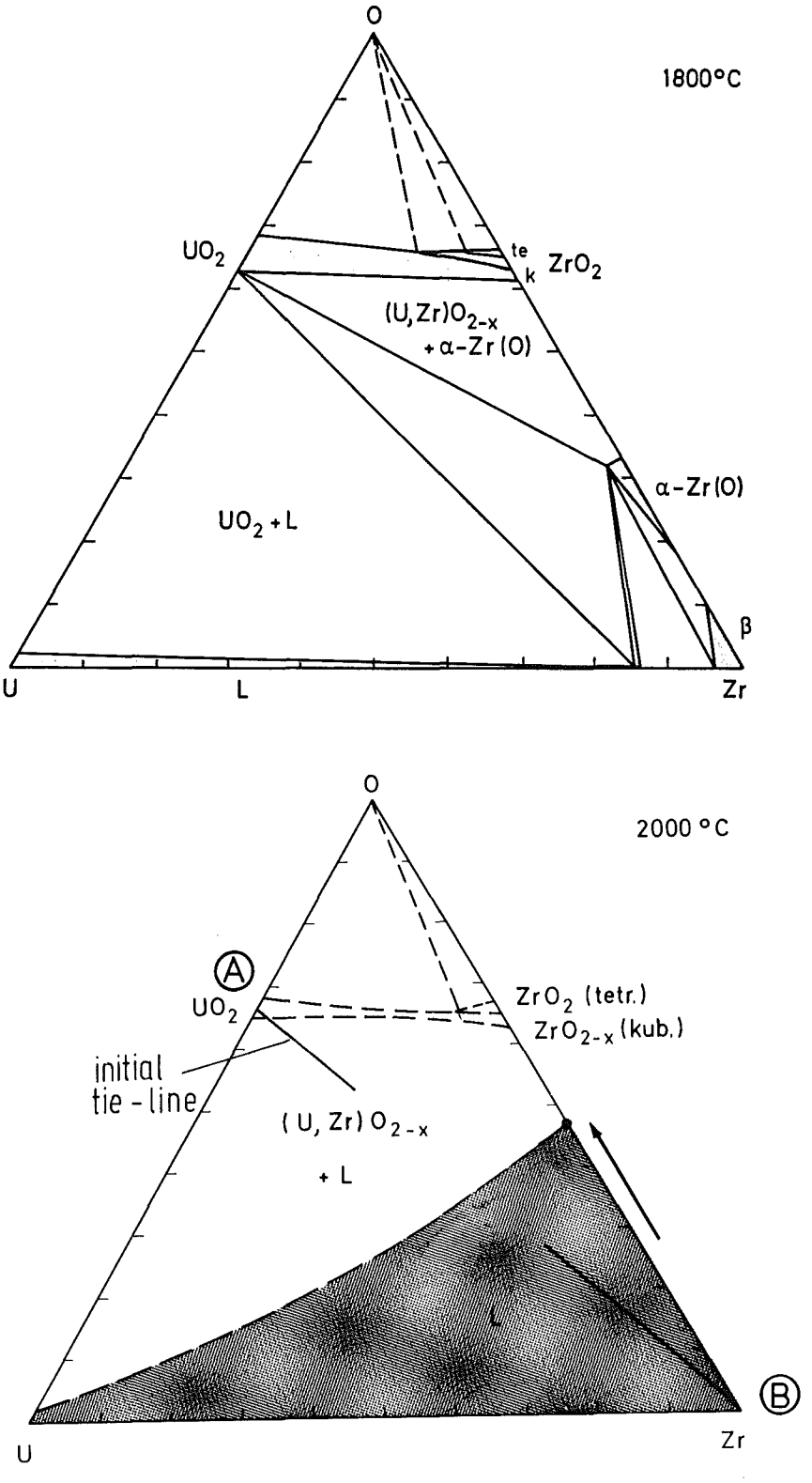

Fig. 18: Isothermal sections of the ternary U-Zr-O system at 1800 and 2000 °C.

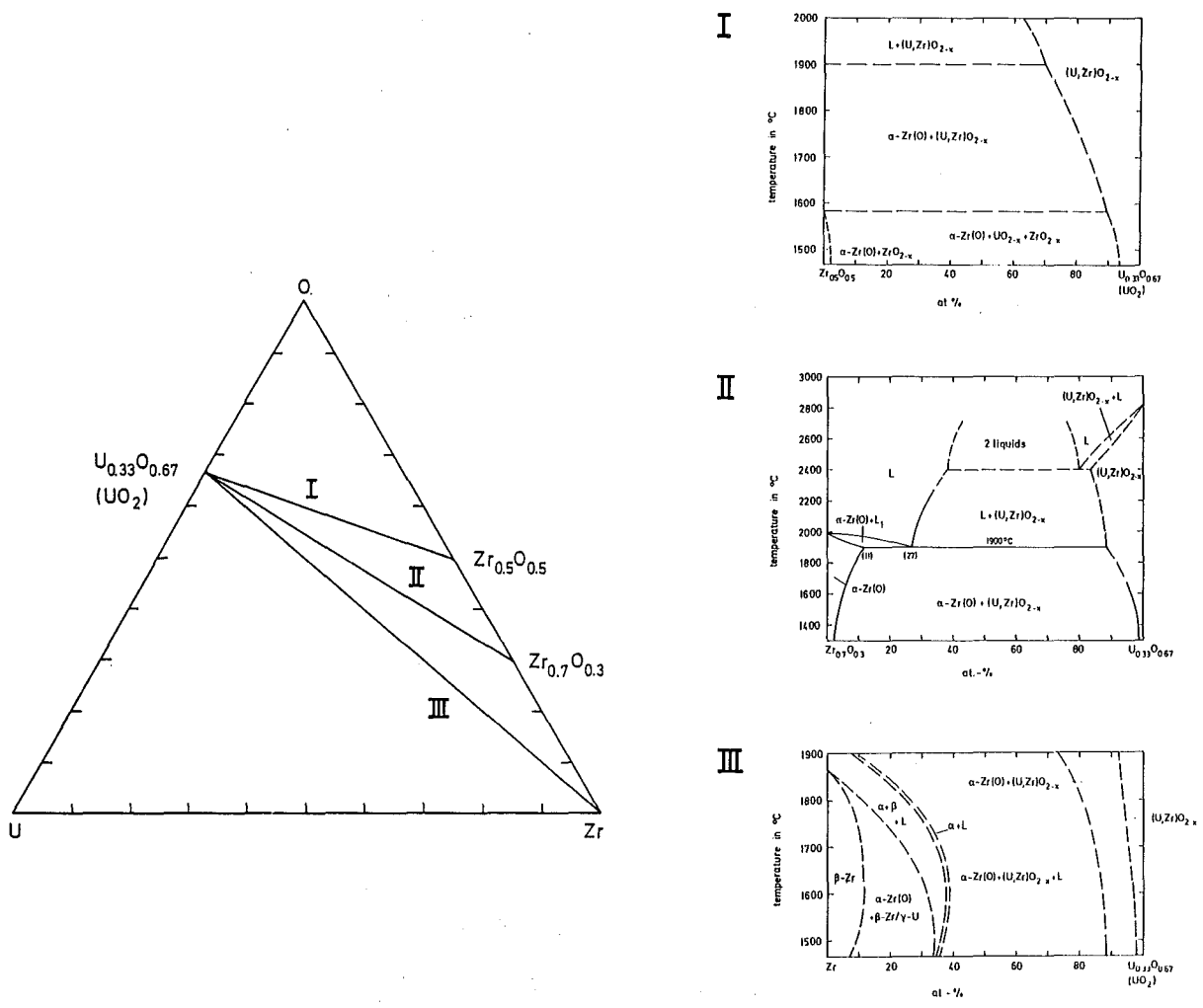

Fig. 19: Tentative temperature-concentration diagrams (in at.%) of the ternary joins: I = $Zr_{0.5}O_{0.5}$-UO_2, II = $Zr_{0.7}O_{0.3}$ [α-Zr(O)]-UO_2, III = Zr-UO_2.

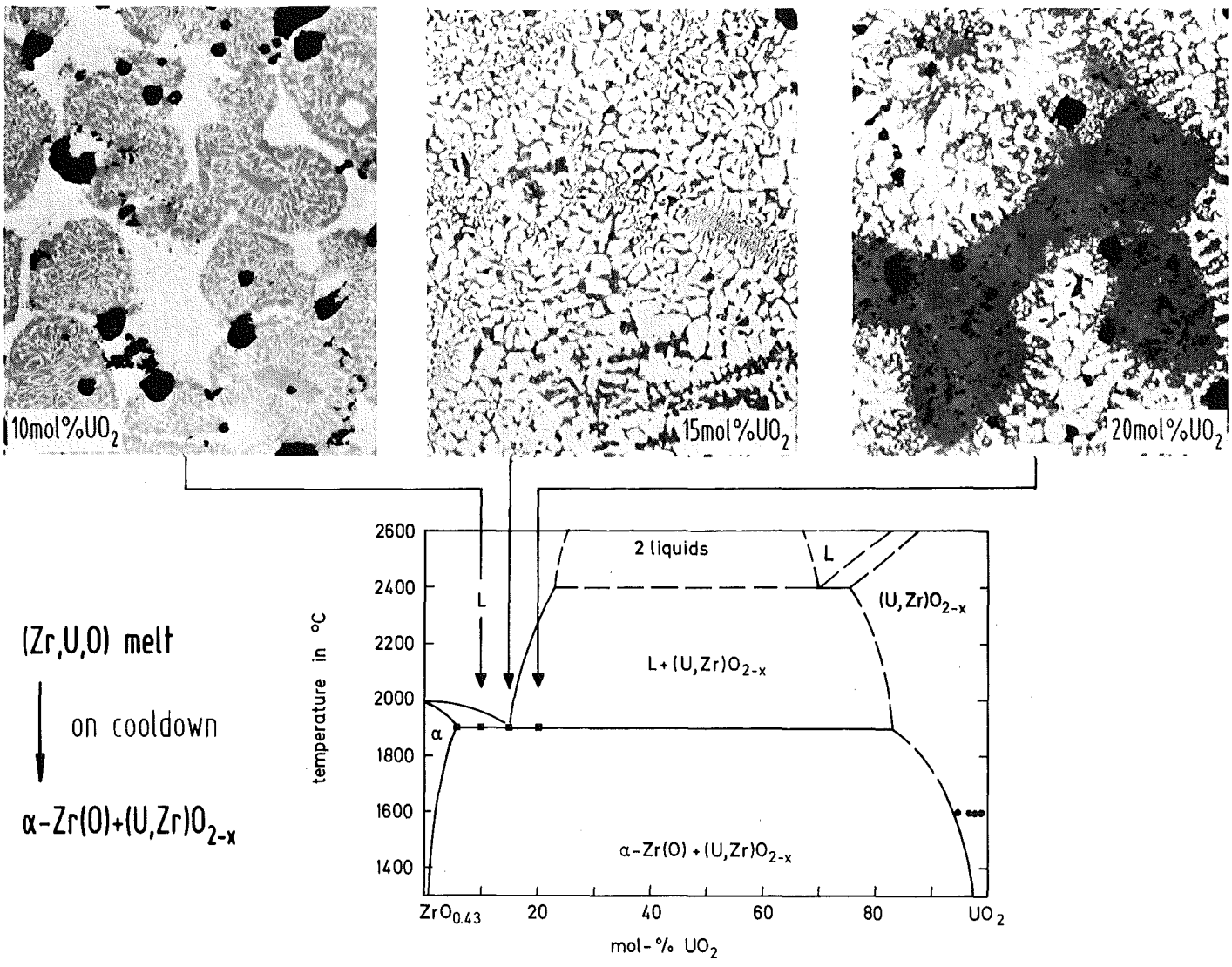

Fig. 20: Temperature concentration diagram of the quasibinary α-Zr(O)-UO_2 system in mol.%. Typical microstructures of melt specimens with hypoeutectic, eutectic [α-Zr(O)/UO_2] and hypereutectic composition.

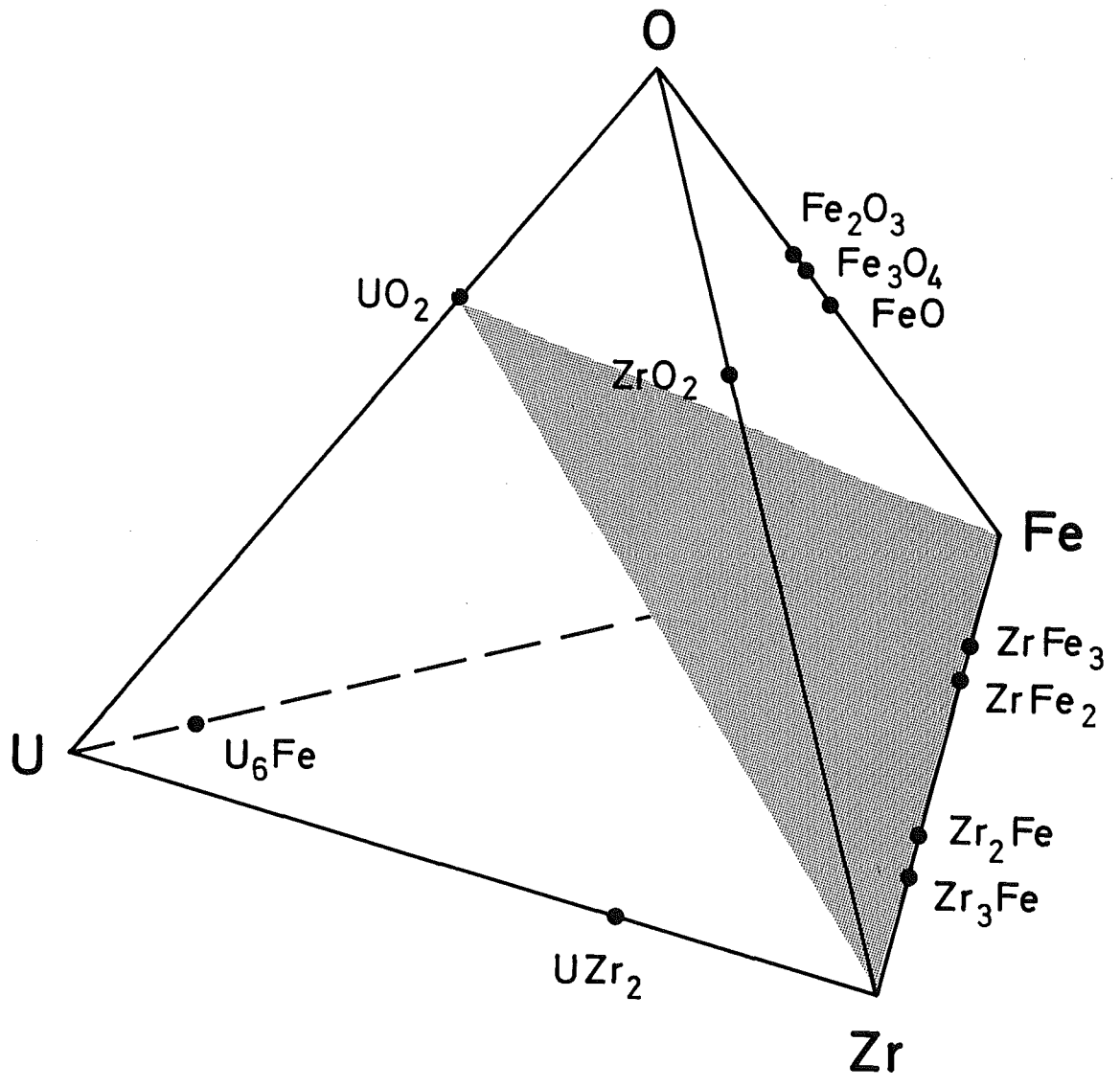

Fig. 21: Position of the UO_2-Zr-Fe section in the quaternary U-Zr-Fe-O system (schematic).

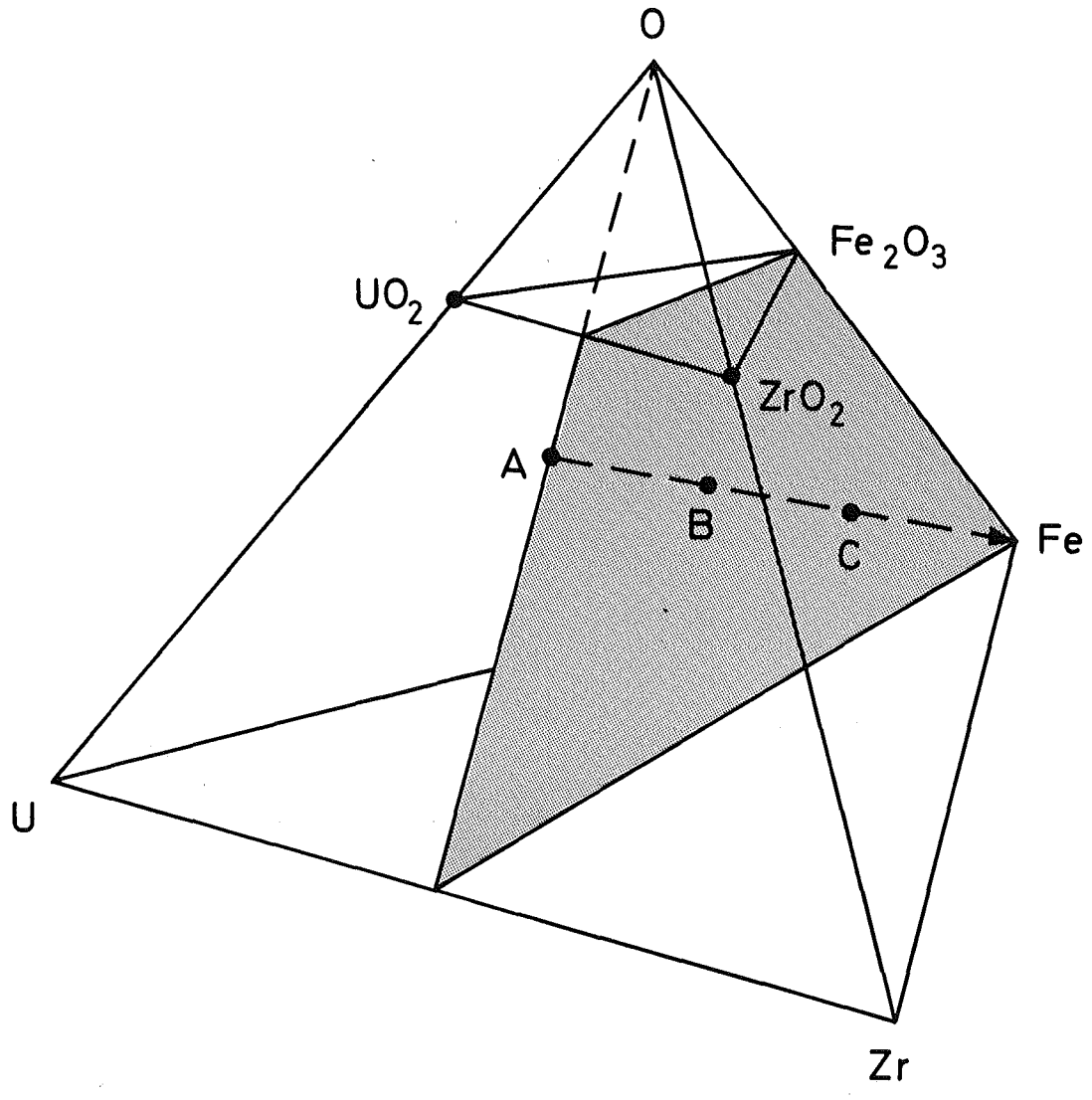

Fig. 22: Position of the $U_{0.5}Zr_{0.5}$-Fe-O section in the quaternary U-Zr-Fe-O system (schematic).

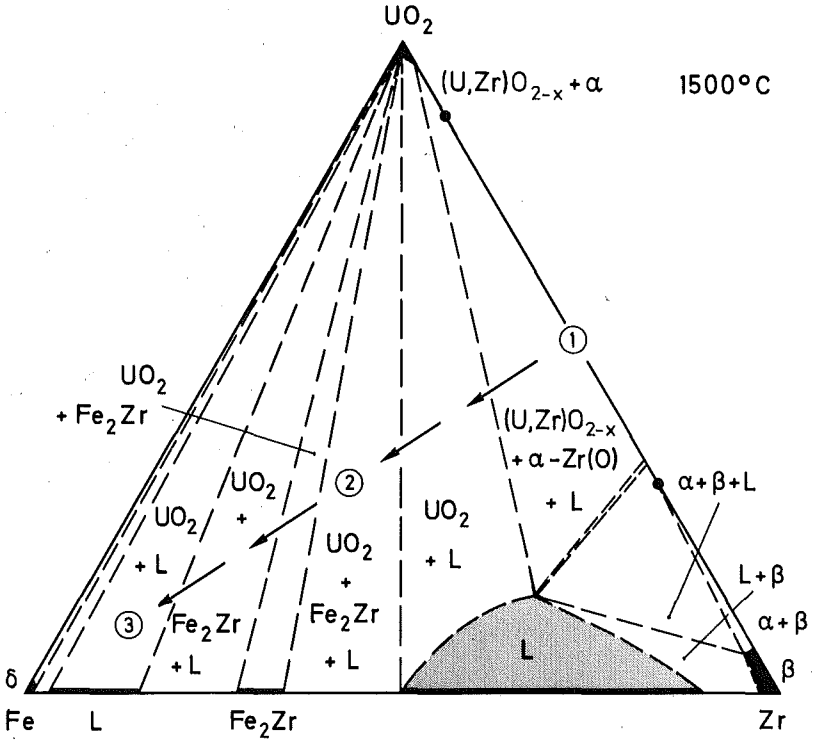

Fig. 23: Tentative isothermal quaternary section UO_2-Zr-Fe at 1500 °C (compositions: 1 = fuel rod, 2 = "Corium A", 3 = "Corium E").

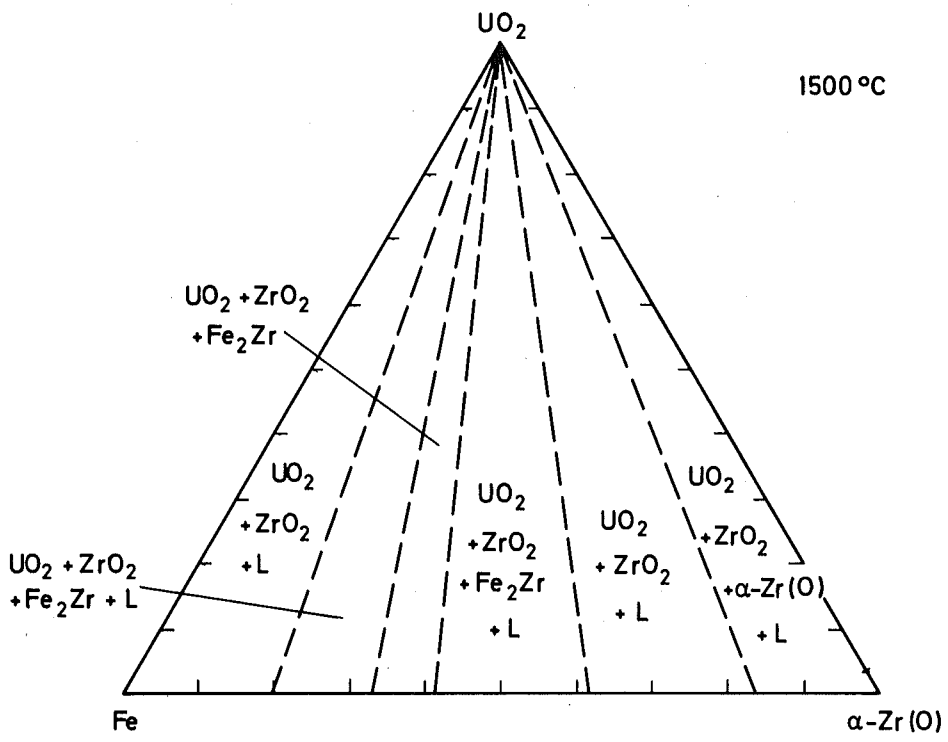

Fig. 24: Tentative isothermal quaternary section UO_2-α-Zr(O)-Fe at 1500 °C.

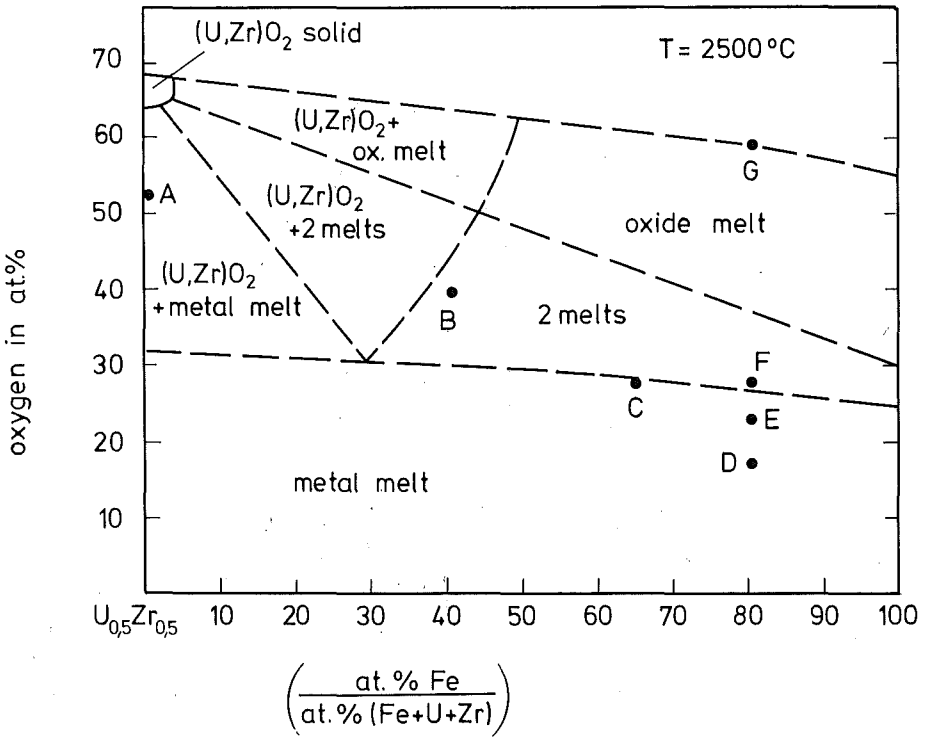

Fig. 25: Assessed phase regions in the section $(U_{0.5}Zr_{0.5})$-Fe-O at 2500 °C. (A = fuel rod, B = "Corium A", C = "Corium" A + E 1:1, D = "Corium E", E = D + F 1:1, F = "Corium E" partially oxidized, G = "Corium E" totally oxidized).

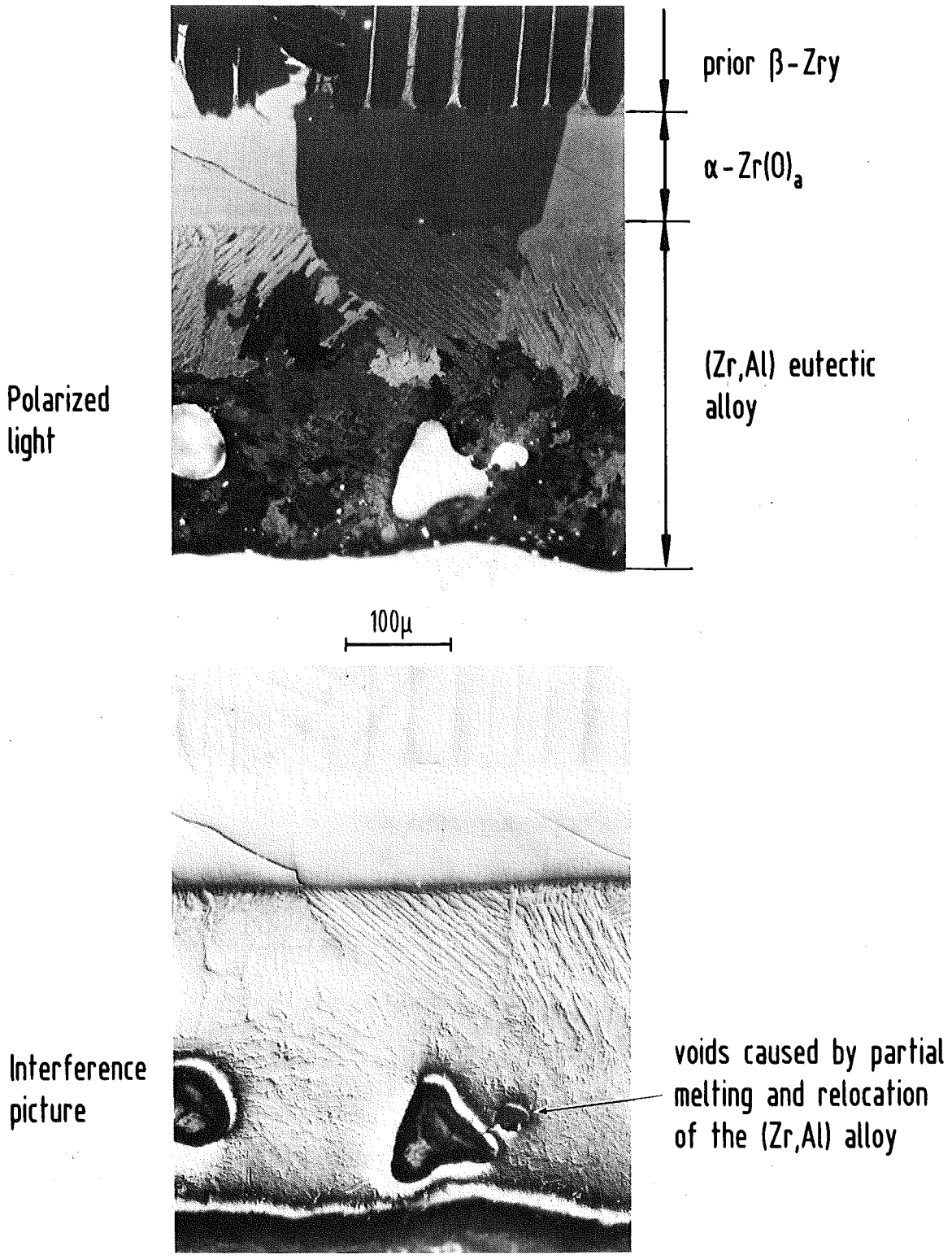

Fig 26: Sequence of Zircaloy-4/Al_2O_3 reaction layers after annealing at 1400 °C for 30 min. The (Zr,Al) alloy which forms as result of the interaction was partially molten.

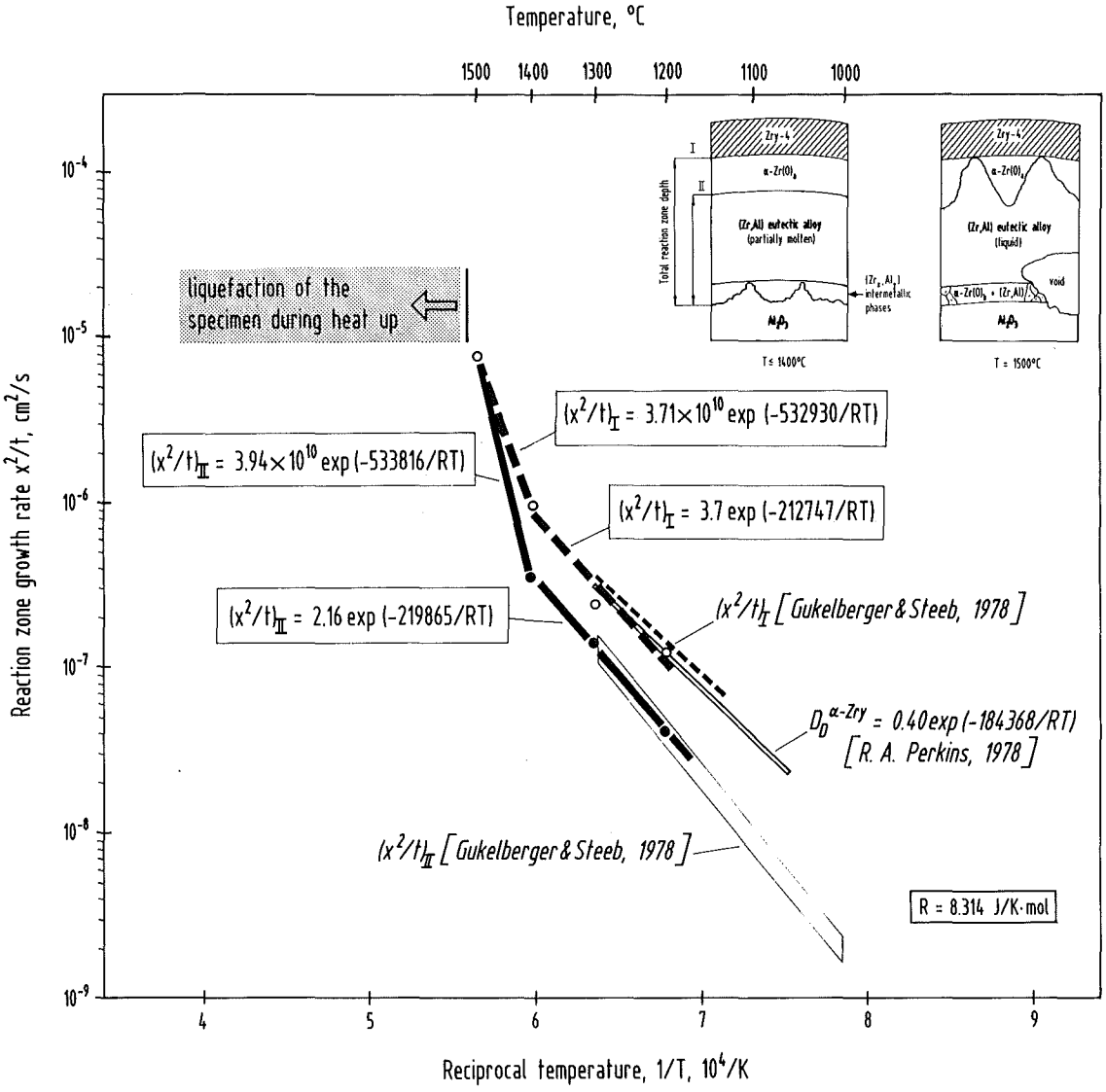

Fig. 27: Reaction zone growth rates in the Zircaloy-4/Al_2O_3 diffusion couple as function of the reciprocal temperature. Comparison with literature data and the oxygen diffusion coefficient in α-Zr(O).

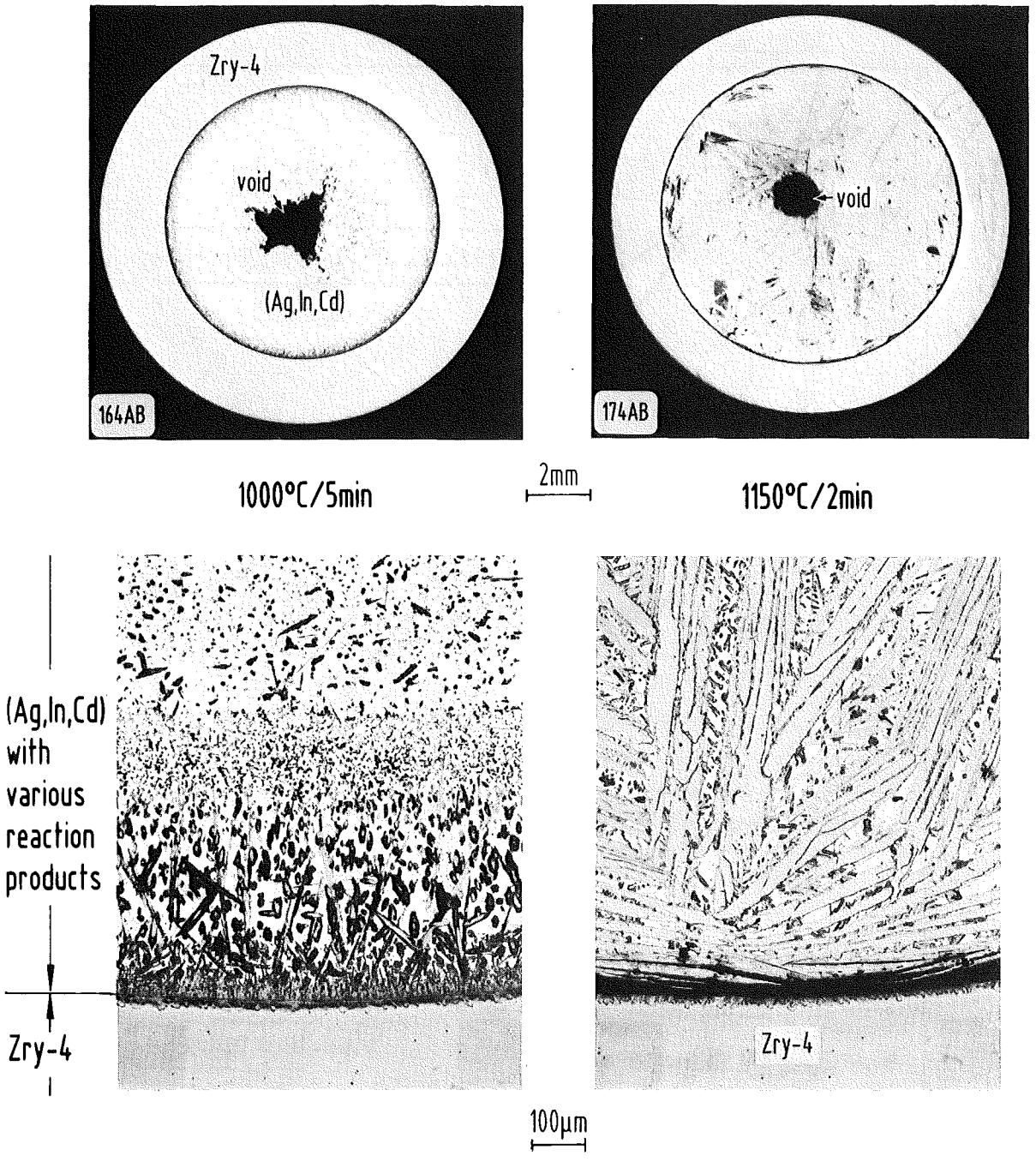

Fig. 28: Chemical interactions between Zircaloy and the PWR absorber rod material (Ag, In,Cd). The Zircaloy has been chemically dissolved to a great extent.

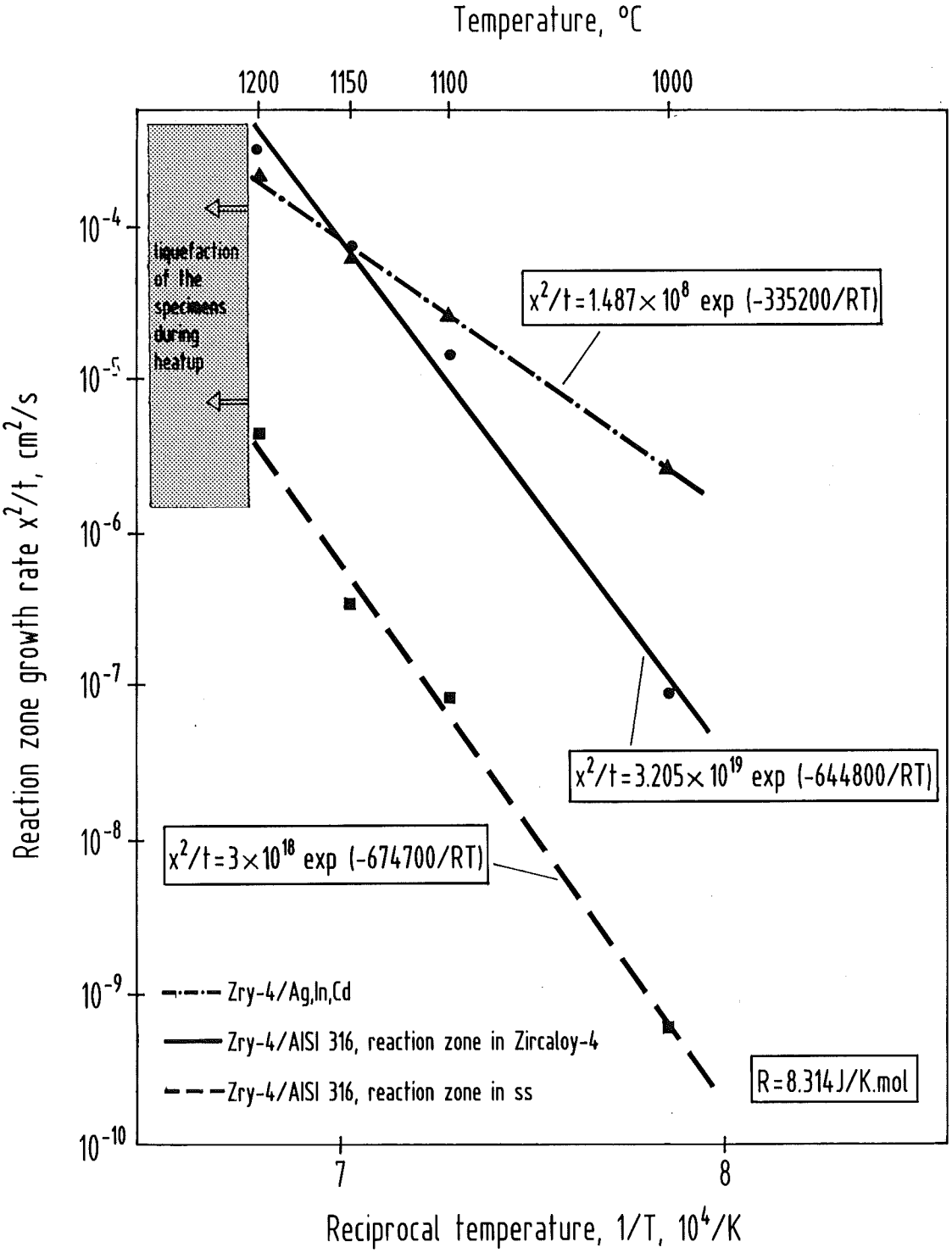

Fig. 29: Reaction zone growth rates of the diffusion couples Zircaloy/(Ag,In,Cd) and Zircaloy/stainless steel AISI 316. In the diffusion couple Zircaloy/AISI 316 one has to distinguish between a reaction zone in Zircaloy and one in stainless steel, respectively.

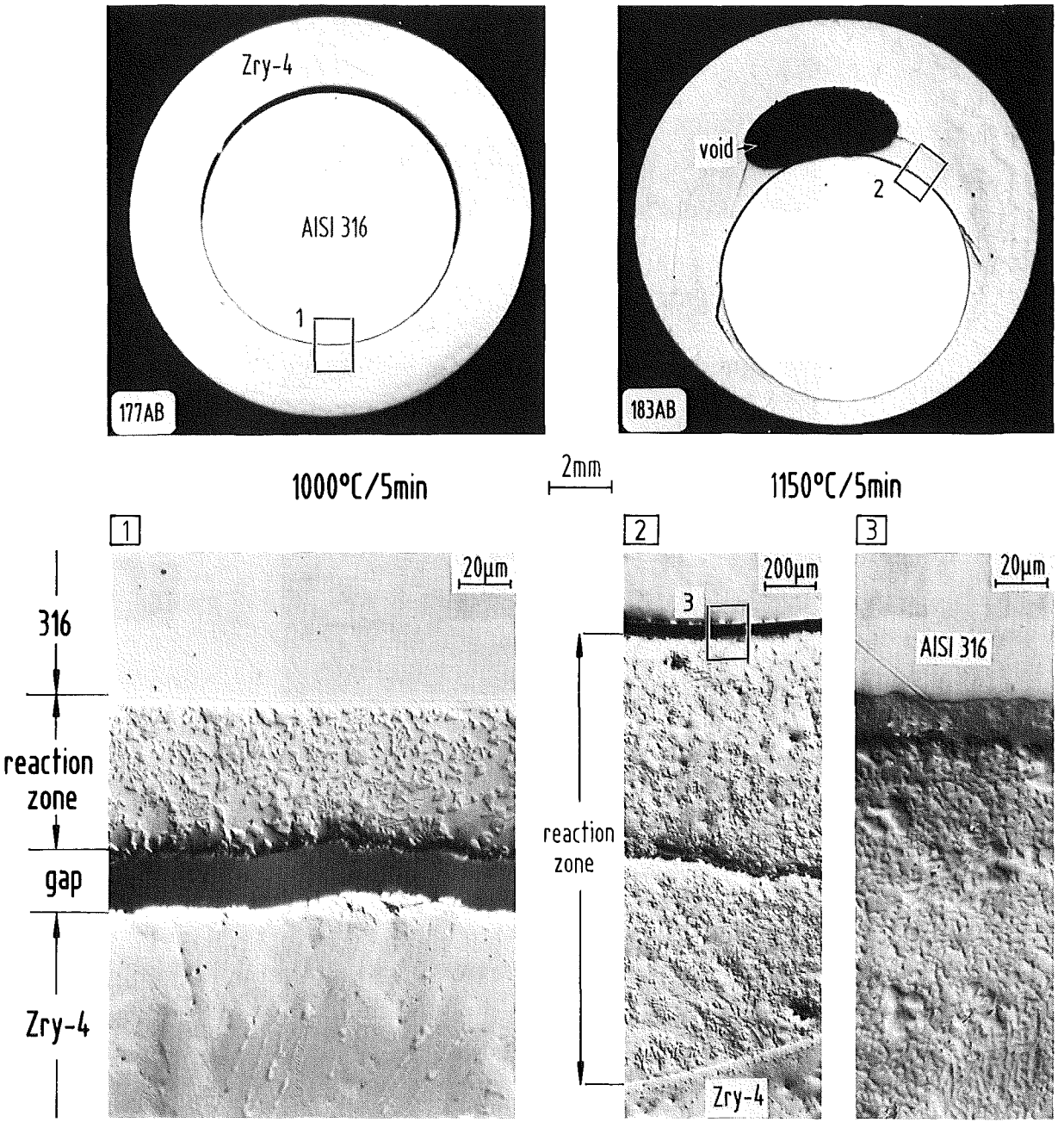

Fig. 30: Chemical interaction between Zircaloy and stainless steel AISI 316. At 1150 °C liquid phases form which partially relocate and form voids.

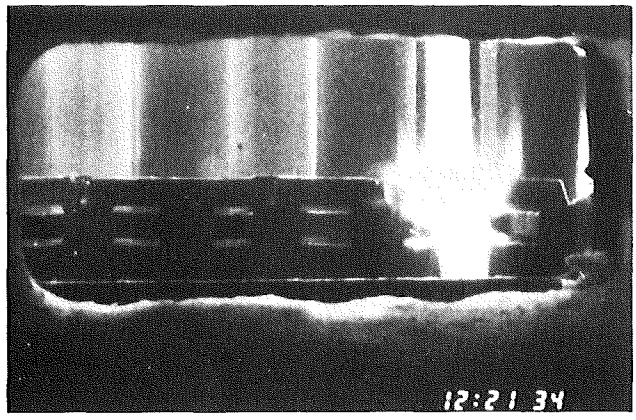

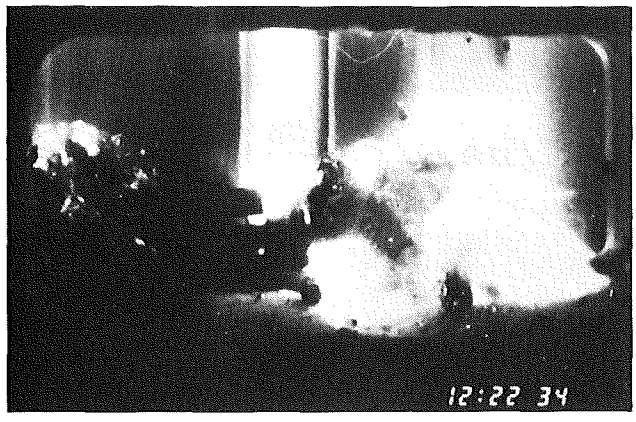

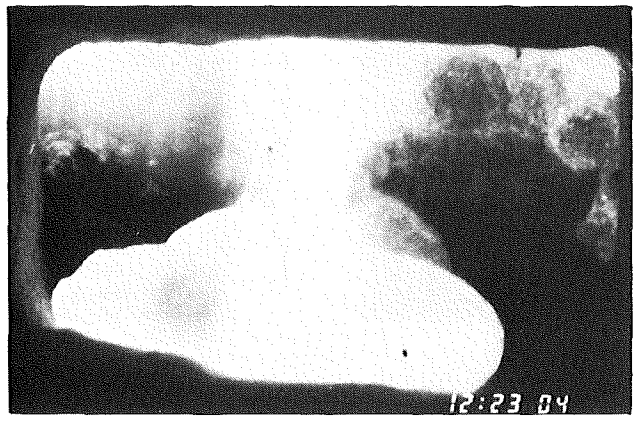

Fig. 31: Accummulation of an (Ag,In,Cd) absorber rod melt at the elevation of the Inconel grid spacer (500 mm) in the test CORA-5. The pictures are taken during the experiment by a video system through a window in the shroud.

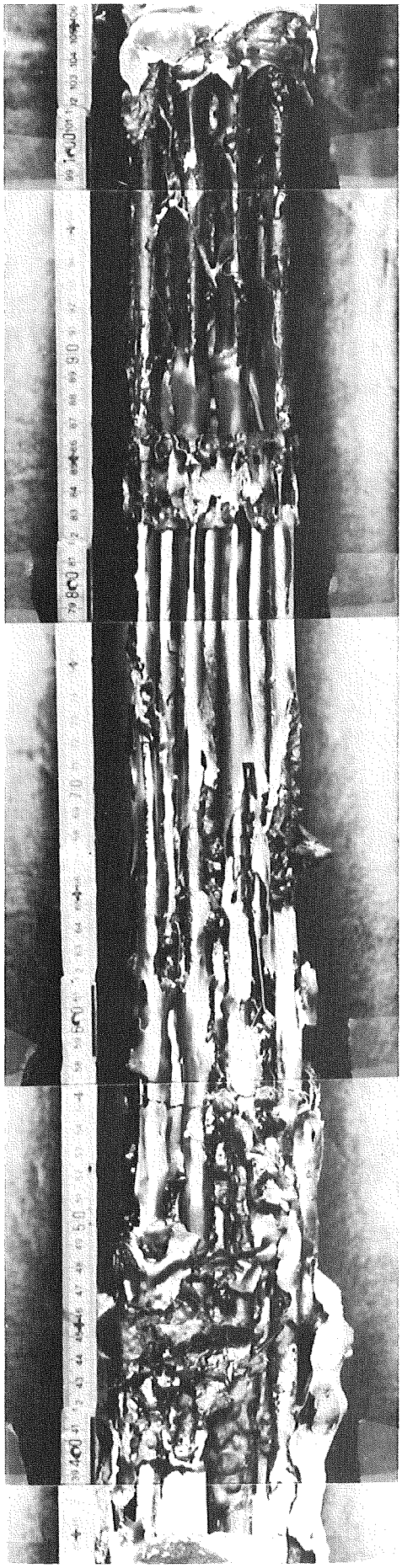

Fig. 32: Post-test appearance of bundle CORA-5 ($T_{max} \approx 2000$ °C, 1 (Ag,In,Cd) absorber rod) after removal of the insulation and shroud.

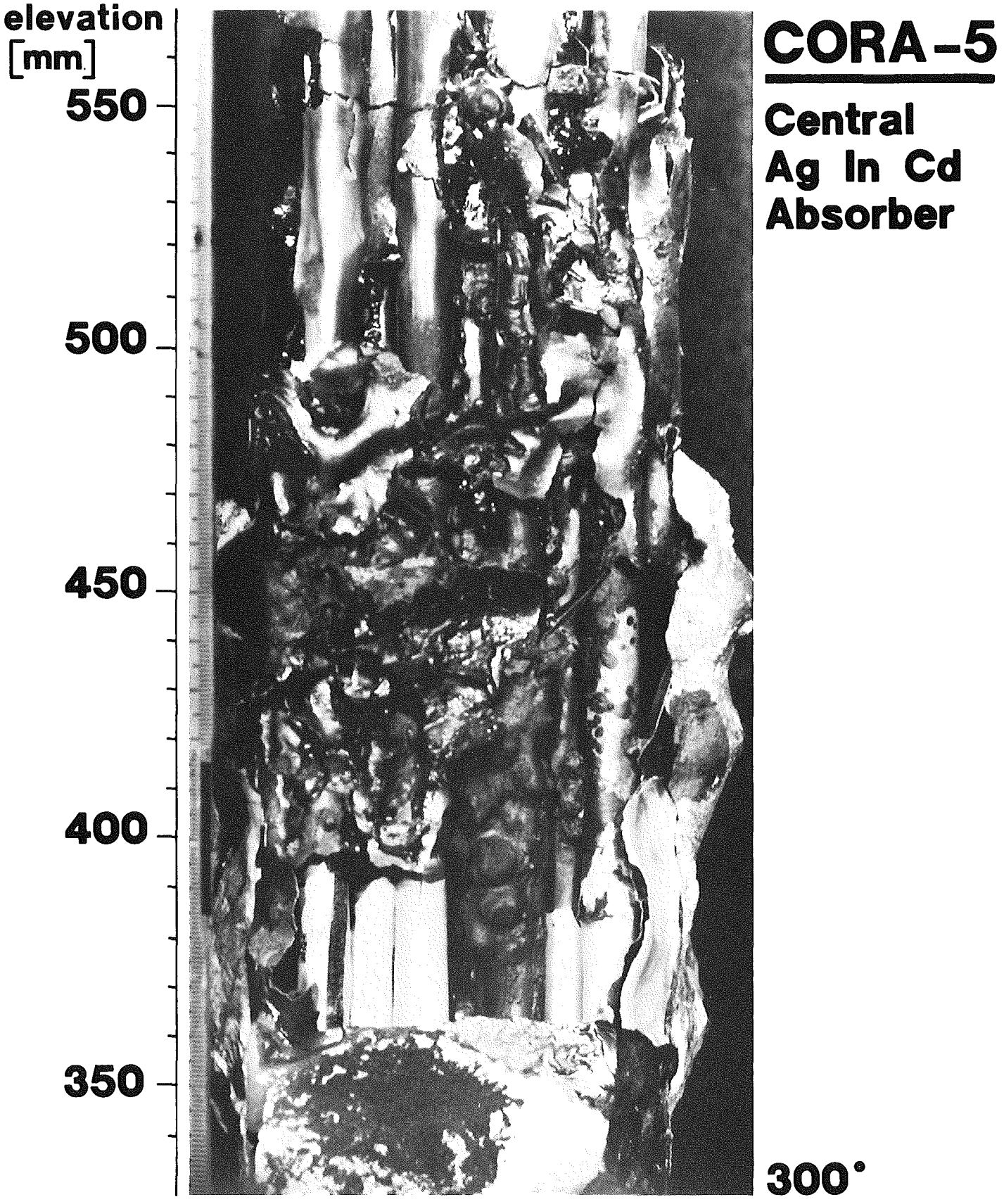

Fig. 33: Some details of the center region of the bundle CORA-5 after the test. Beside relocated melts one can recognize embrittled cladding material and fuel fragments.

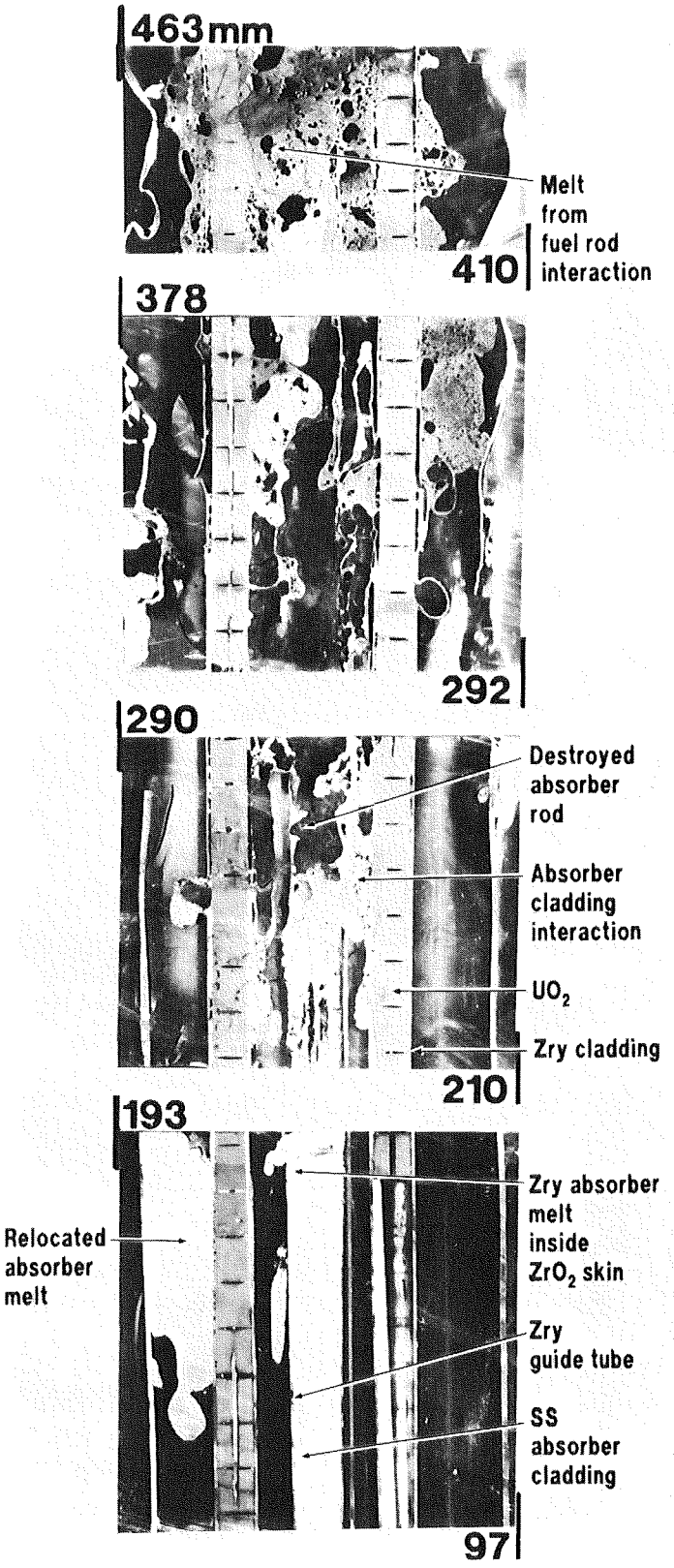

Fig. 34: Some vertical cross-sections of the bundle CORA-5 at the elevations indicated. The central absorber rod has disappeared in the upper part of the bundle.

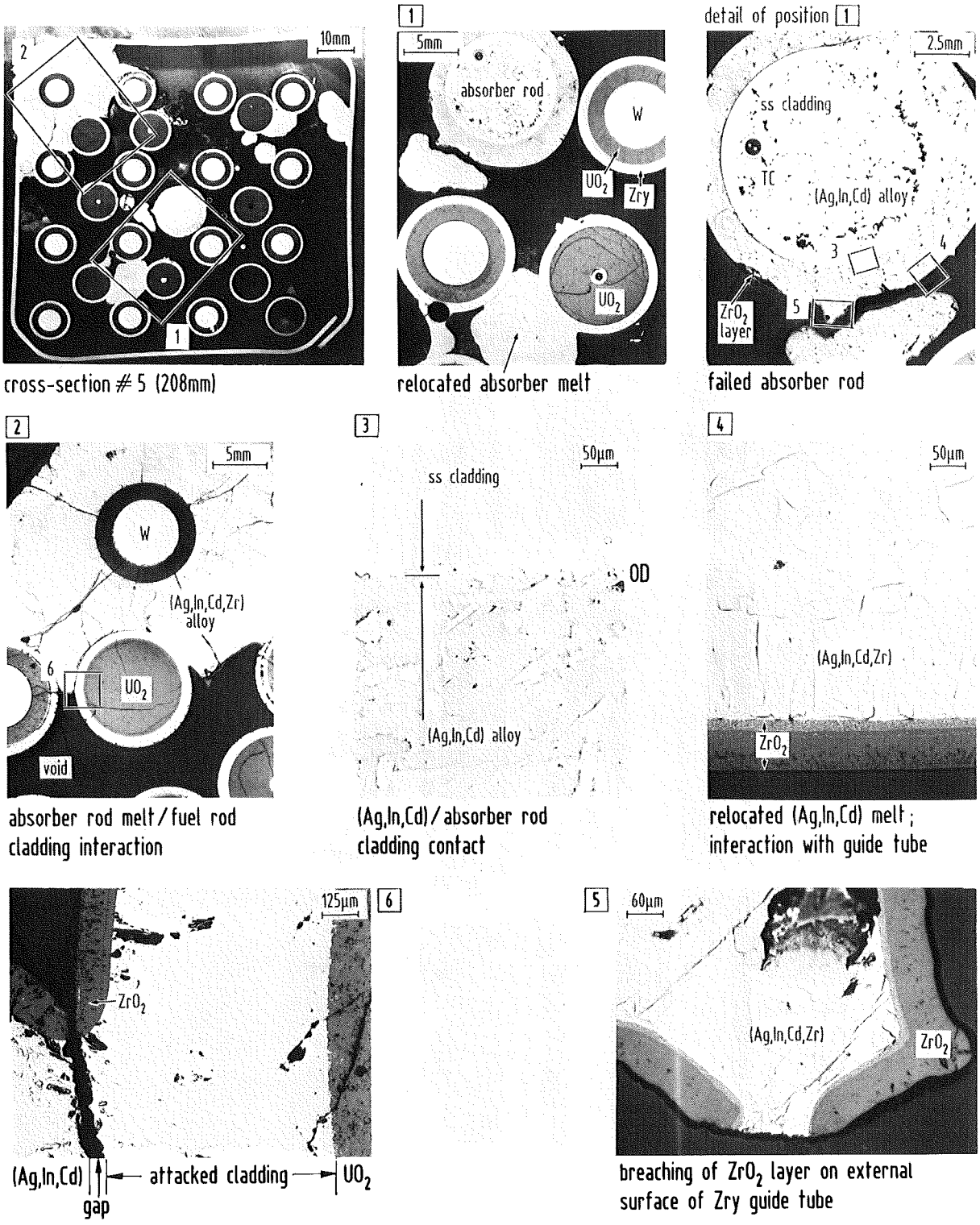

Fig. 35: Macro- and microstructure of CORA bundle 5 at the cross-section elevation 208 mm. Whereas the stainless steel cladding of the absorber rod is still intact the Zry guide tube is to a great extent dissolved (detail of position 1).

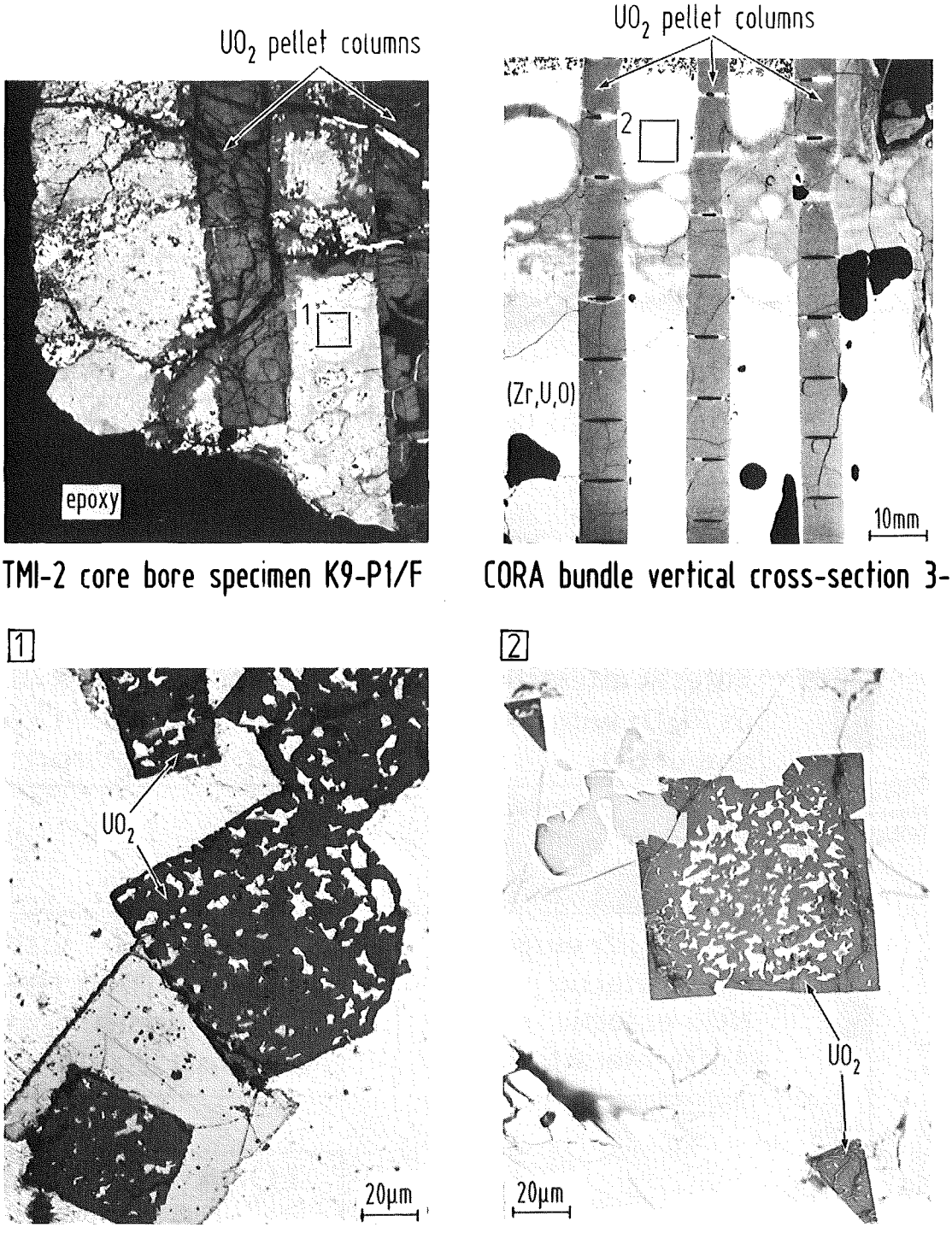

Fig. 36: Comparison of the microstructure seen during the examination of the TMI-2 core bore specimen K9-PI/F and of CORA bundle 3 cross-sections. Formation of large UO_2 particles in a metallic melt.

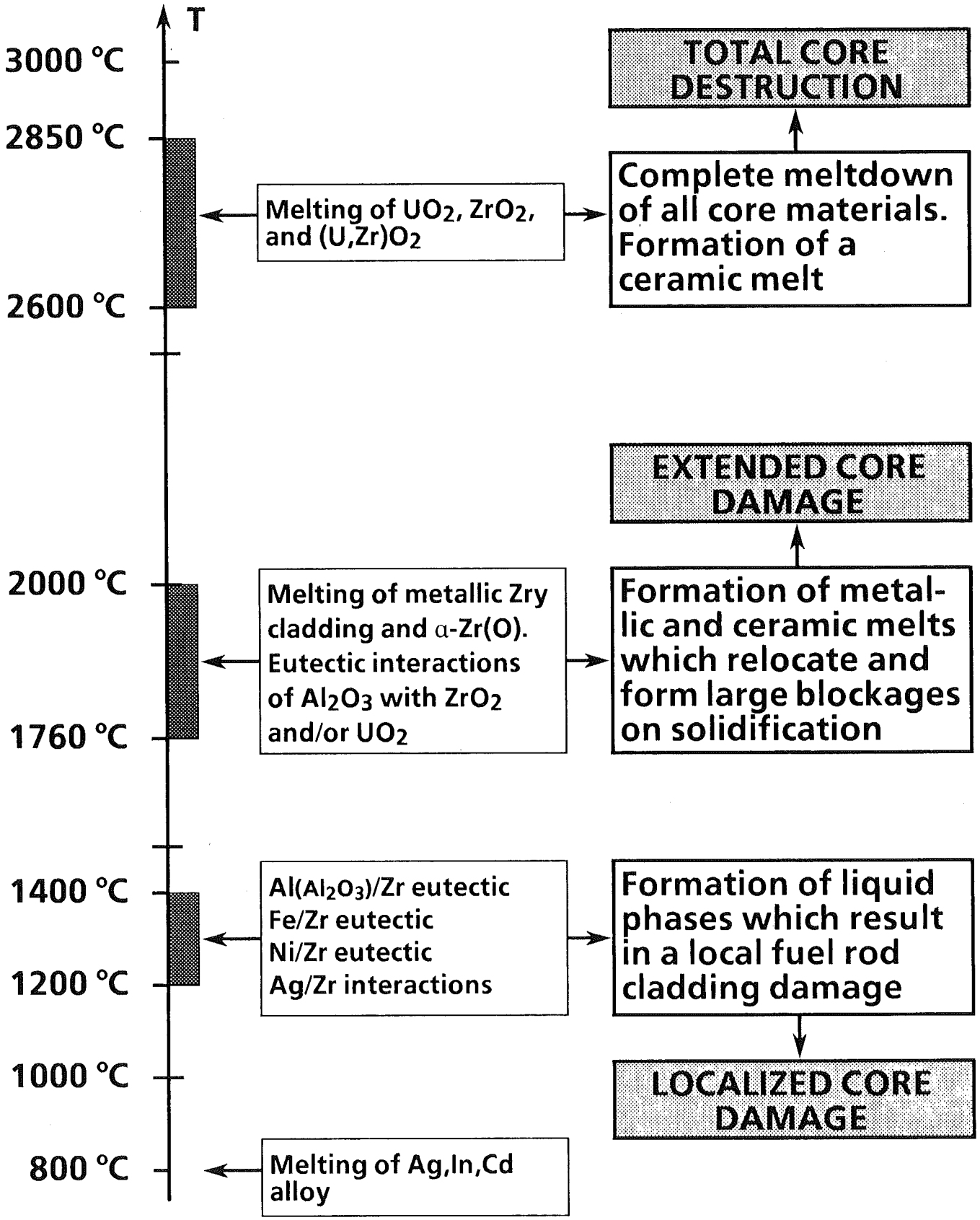

Fig. 37: Temperature regimes for liquid phase formations in a severe reactor accident and possible consequences on reactor core damage.